

Entangling Schrödinger's cat states by bridging discrete- and continuous-variable encoding

Daisuke Hoshi,^{1, 2, *} Toshiaki Nagase,^{1, 2, *} Sangil Kwon,^{3, *} Daisuke Iyama,^{1, 2} Takahiko Kamiya,^{1, 2} Shiori Fujii,^{1, 2} Hiroto Mukai,^{2, 3} Shah Nawaz Ahmed,⁴ Anton Frisk Kockum,⁴ Shohei Watabe,^{3, 5} Fumiki Yoshihara,^{1, 3} and Jaw-Shen Tsai^{2, 3, 6}

¹*Department of Physics, Graduate School of Science, Tokyo University of Science, 1-3 Kagurazaka, Shinjuku-ku, Tokyo 162-8601, Japan*

²*RIKEN Center for Quantum Computing (RQC), Wako-shi, Saitama 351-0198, Japan*

³*Research Institute for Science and Technology, Tokyo University of Science, 1-3 Kagurazaka, Shinjuku-ku, Tokyo 162-8601, Japan*

⁴*Department of Microtechnology and Nanoscience, Chalmers University of Technology, 412 96 Gothenburg, Sweden*

⁵*College of Engineering, Shibaura Institute of Technology, 3-7-5 Toyosu, Koto-ku, Tokyo 135-8548, Japan*

⁶*Graduate School of Science, Tokyo University of Science, 1-3 Kagurazaka, Shinjuku-ku, Tokyo 162-8601, Japan*

(Dated: January 22, 2025)

In quantum information processing, two primary research directions have emerged: one based on discrete variables (DV) and the other on the structure of quantum states in a continuous-variable (CV) space. Integrating these two approaches could unlock new potentials, overcoming their respective limitations. Here, we show that such a DV–CV hybrid approach, applied to superconducting Kerr parametric oscillators (KPOs), enables us to entangle a pair of Schrödinger's cat states by two methods. The first involves the entanglement-preserving conversion between Bell states in the Fock-state basis (DV encoding) and those in the cat-state basis (CV encoding). The second method implements a \sqrt{iSWAP} gate between two cat states following the procedure for Fock-state encoding. This simple and fast gate operation completes a universal quantum gate set in a KPO system. Our work offers powerful applications of DV–CV hybridization and marks a first step toward developing a multi-qubit platform based on planar KPO systems.

I. INTRODUCTION

For nearly three decades, there have been two paradigms in quantum information processing: one involves discrete variables (DVs), such as photon number (Fock) states or spin states [1–4], whereas the other relies on the structure of quantum states in a continuous-variable (CV) space, such as Schrödinger's cat and Gottesman–Kitaev–Preskill states [5–7]. Recently, considerable efforts have focused on bridging DV and CV quantum information to overcome the limitations of each paradigm [8–15]. Parametrically driven Kerr nonlinear resonators, often referred to as Kerr parametric oscillators (KPOs) [16–20], offer a unique testbed for this task, particularly for exploring emergent quantum properties like entanglement in interacting quantum systems. This capability is enabled by simple one-to-one conversion between Fock and cat states via parametric pump control [21–28].

In our previous work [29], we experimentally demonstrated that such conversion in a superconducting planar KPO preserves the quantum coherence of the system, with the underlying physics being quantum tunnelling in phase space [30, 31]. Furthermore, we showed that single-gate operations on cat states in a KPO can be implemented similarly to conventional gate operations on the Fock-state basis [32–38].

To establish KPO systems as a promising quantum information platform, the next step would be extending our approach to a multi-KPO system. Although there have been studies on two interacting KPOs [39–41], the entanglement between them and its preservation during the conversion between Fock and cat states have yet to be investigated. Additionally, the two-KPO gate operation for cat-state encoding, which we refer to as the two-cat gate, has not been demonstrated.

In this work, we introduce two straightforward methods to create entangled cat states—a valuable resource for fault-tolerant quantum computation and communication [42–48]—by bridging DV and CV domains. The first method is the entanglement-preserving and deterministic conversion from Fock-state encoding to cat-state encoding. Such a conversion suggests the possibility of constructing quantum networks in the cat basis using conventional schemes originally developed for the Fock basis, thereby reducing experimental complexity. Thus, our demonstration highlights the potential of DV–CV hybridization and may lay new groundwork for constructing quantum networks in the cat basis.

The next method is to implement a \sqrt{iSWAP} gate between two cat states in a manner almost identical to that for Fock-state encoding [49]. This allows us to create entangled cat states faster than previous implementations on bosonic modes [50, 51], using only a single square pulse. Our implementation completes the demonstration of a universal quantum gate set,

* These authors contributed equally to this work.
email: kwon2866@gmail.com (Sangil Kwon)

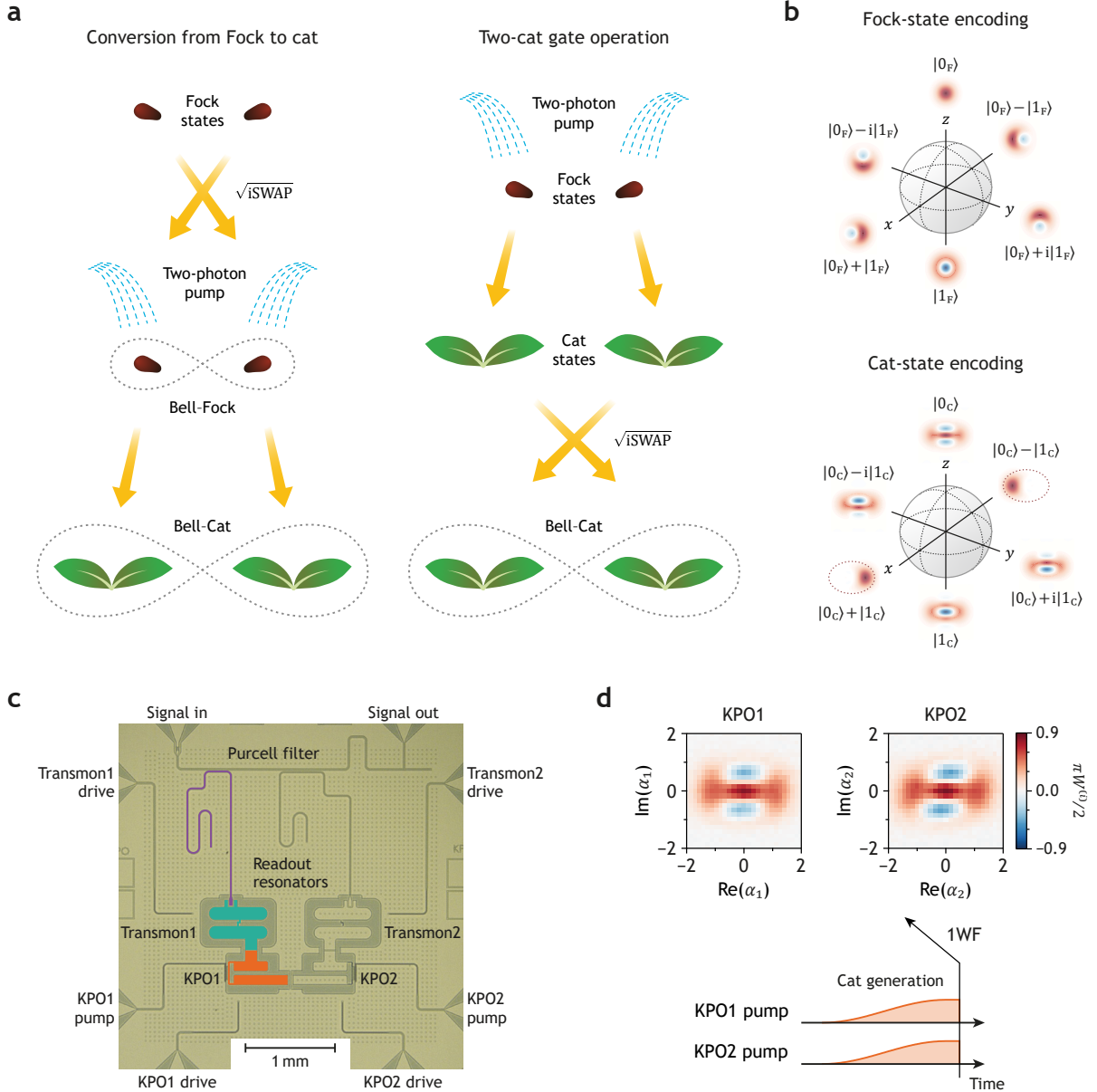


Fig. 1: Concept of the experiment. **a** Seed-sprout analogy for our methods to create Bell-Cat states. In this analogy, the seeds represent Fock state encoding, the sprouts represent cat state encoding, water sprinkles represent two-photon pumps, and gray dotted curves indicate entanglement. The normalization factor was omitted for simplicity. **b** Bloch spheres for Fock state encoding and cat state encoding. The left side is in false colour for clarity. Each KPO is composed of 10 direct-current superconducting quantum interference devices (DC SQUIDs) with a shunting capacitor. The two KPOs are capacitively coupled. The state of each KPO is monitored by the nearby transmon (green) and its readout resonator (purple). **c** Figure of the chip. The left side is in false colour for clarity. Each KPO is composed of 10 direct-current superconducting quantum interference devices (DC SQUIDs) with a shunting capacitor. The two KPOs are capacitively coupled. The state of each KPO is monitored by the nearby transmon (green) and its readout resonator (purple). **d** Simultaneous and independent generation of even cat states $|0_c\rangle$ from vacuum states $|0_F\rangle$ and the corresponding pulse sequence. The pulse sequence used to measure the Wigner function is omitted for simplicity (see Supplementary Fig. 2 for the full pulse sequence). The colour represents the scaled one-mode Wigner function (1WF), i.e., the number parity.

alongside the single-cat gate operations from our previous work [29].

For both our methods, we can make analogies to seeds (from the DV domain) sprouting (in the CV domain) thanks to watering (two-photon pumping), as illustrated in Fig. 1a. In this paper, we denote Fock states $|0\rangle$ and $|1\rangle$ as $|0_F\rangle$ and $|1_F\rangle$, respectively. Correspondingly, the even and odd cat states are denoted as $|0_c\rangle$ and $|1_c\rangle$ as shown in Fig. 1b. In addition, we

refer to the Bell states in the Fock basis as Bell-Fock states and designate the resulting entangled cat states as Bell-Cat states.

II. RESULTS

A. Setup

The chip used in this work is shown in Fig. 1c. It is the same chip used in our previous study [29]. The transition frequencies between the $|0\rangle$ and $|1\rangle$ states of the KPOs are 2.564 GHz (KPO1) and 2.420 GHz (KPO2). The self-Kerr coefficient of both KPOs is approximately 2 MHz after ramping up the pump.

The Hamiltonian of our system can be described as (see Sec. 1 of Supplementary Information for the derivation)

$$\begin{aligned} \hat{\mathcal{H}}(t) = & \Delta_1 \hat{a}_1^\dagger \hat{a}_1 - \frac{K_1}{2} \hat{a}_1^\dagger \hat{a}_1^\dagger \hat{a}_1 \hat{a}_1 + \frac{P_1(t)}{2} (\hat{a}_1^\dagger \hat{a}_1^\dagger + \hat{a}_1 \hat{a}_1) \\ & + \Delta_2 \hat{a}_2^\dagger \hat{a}_2 - \frac{K_2}{2} \hat{a}_2^\dagger \hat{a}_2^\dagger \hat{a}_2 \hat{a}_2 + \frac{P_2(t)}{2} (\hat{a}_2^\dagger \hat{a}_2^\dagger + \hat{a}_2 \hat{a}_2) \\ & + g (\hat{a}_1^\dagger \hat{a}_2 e^{+i\Delta_p t} + \hat{a}_1 \hat{a}_2^\dagger e^{-i\Delta_p t}). \end{aligned} \quad (1)$$

Here, we are working in units where $\hbar = 1$; \hat{a}_i and \hat{a}_i^\dagger are the ladder operators for the KPO*i* ($i = 1, 2$); $\Delta_i (\equiv \omega_{K_i} - \omega_{p_i}/2)$ is the KPO-pump frequency detuning, where ω_{K_i} is the transition frequency between the $|0_F\rangle$ and $|1_F\rangle$ states, and ω_{p_i} is the frequency of the two-photon pump; K_i is the self-Kerr coefficient; P_i is the amplitude of the pump; g is the coupling constant; and $\Delta_p [\equiv (\omega_{p1} - \omega_{p2})/2]$ is half of the detuning between the two pumps. The Hamiltonian in Eq. (1) is in the rotating frame defined by $\hat{\mathcal{H}}_0 = \sum_i (\omega_{p_i}/2) \hat{a}_i^\dagger \hat{a}_i$. See Supplementary Table 1 for the values of these system parameters.

The cat states are generated adiabatically using the pump pulse with the profile $\sin^2(\pi t/2\tau_{\text{ramp}})$, where the ramping time τ_{ramp} is 1 μs (see Methods for more details). Throughout this work, for both KPOs, the P/K ratio is chosen to be 1.0, and the pump detuning [Δ_1 and Δ_2 in Eq. (1)] is chosen to be 1.0 MHz. Since the detuning between the two KPOs (144 MHz) is nearly 20 times larger than the coupling (8 MHz), the interaction is effectively turned off on the timescale of the measurements; thus, cat states can be generated and measured independently and simultaneously as shown in Fig. 1d.

B. Conversion from Fock to cat

We first prepare all four types of Bell-Fock state, $|0_F0_F\rangle \pm |1_F1_F\rangle$ and $|0_F1_F\rangle \pm |1_F0_F\rangle$. Subsequent two-photon pumping to each KPO converts the Bell-Fock state into the same type of Bell-Cat state; for instance, from $|0_F0_F\rangle + |1_F1_F\rangle$ to $|0_C0_C\rangle + |1_C1_C\rangle$ (see Fig. 2c for the pulse sequence). This approach relies on the fundamental property of entanglement, namely, that “entanglement is preserved under local unitary operations” [52].

The Bell-Fock state is prepared by activating the interaction between the KPOs by applying a para-

metric pulse with either the frequency $\omega_{K1} + \omega_{K2}$ or $\omega_{K1} - \omega_{K2}$ to the pump ports [3]. A parametric pulse with each frequency induces the transitions between $|0_F0_F\rangle$ and $|1_F1_F\rangle$, and between $|0_F1_F\rangle$ and $|1_F0_F\rangle$ based on the three-wave mixing capability of our KPOs. Using such transitions, we can create states $|0_F0_F\rangle + e^{i\phi_s} |1_F1_F\rangle$ and $|0_F1_F\rangle + e^{i\phi_d} |1_F0_F\rangle$, where the phases ϕ_s and ϕ_d are determined by the phase of the parametric pulse (virtual Z gate). We refer to this pulse as the Bell-preparation pulse. Rabi oscillations associated with the Bell-preparation pulse are shown in Fig. 2a.

For the full characterization of such entangled quantum states, we measured the two-mode Wigner functions (2WFs) (Fig. 2d,e) [45, 53] because the one-mode Wigner functions (1WFs) cannot provide information on entanglement—all Bell states show the same 1WF, which is identical to that of the fully mixed state (Fig. 2b). The 2WFs of the target Bell-Fock and Bell-Cat states are shown in Supplementary Fig. 3.

We observe all essential features in the 2WF of Bell-Cat states (Fig. 2e). Firstly, in the Re-Re plots with $\text{Im}(\alpha_i) = 0$ ($i = 1, 2$), two red circles aligned diagonally indicate the correlation between the two KPOs, similar to the results in Ref. [39]. The alignment direction of the red circles represents the sign of the superposition. The colour of the centre circle, which represents the joint number parity, indicates the type of Bell state; for instance, $|01\rangle + e^{i\phi} |10\rangle$ shows a blue centre regardless of whether the basis is Fock or cat. Secondly, the interference pattern in the Im-Im plot with $\text{Re}(\alpha_i) = 0$ demonstrates that the correlation is of quantum nature.

Note that the patterns in Fig. 2d,e illustrate how the 2WFs of Bell-Fock states evolve to those of Bell-Cat states: As the pump amplitude increases, the pattern in Fig. 2d elongates along the diagonal axis, eventually resembling the Re-Re plots in Fig. 2e. Regarding the Im-Im plots of Bell-Fock states, those of $|0_F1_F\rangle \pm |1_F0_F\rangle$ are identical to the Re-Re plots, whereas the Im-Im plot of $|0_F0_F\rangle \pm |1_F1_F\rangle$ matches the Re-Re plot of $|0_F0_F\rangle \mp |1_F1_F\rangle$. The Im-Im plots in Fig. 2e can be interpreted as a compressed version of the plots in Fig. 2d along the diagonal axis. These 2WF patterns show the profound connection between quantum correlations in the Bell-Fock and Bell-Cat states.

The fidelity between the target and measured Bell-Fock states is 0.81 ± 0.01 (with the error representing the standard deviation); for the Bell-Cat states, the fidelity is 0.60 ± 0.04 . This value would be 0.25 for completely mixed cat states. These fidelities were obtained by reconstructing the density matrix from the measured one- and two-mode Wigner functions (see Methods).

The most notable difference between the 2WFs of the measured and target Bell-Cat states is that the measured states show weaker contrast in the centre circle of the Re-Re plots with $\text{Im}(\alpha_i) = 0$ ($i = 1, 2$) and in the interference pattern of the Im-Im plots with $\text{Re}(\alpha_i) = 0$ compared to the target states. (The

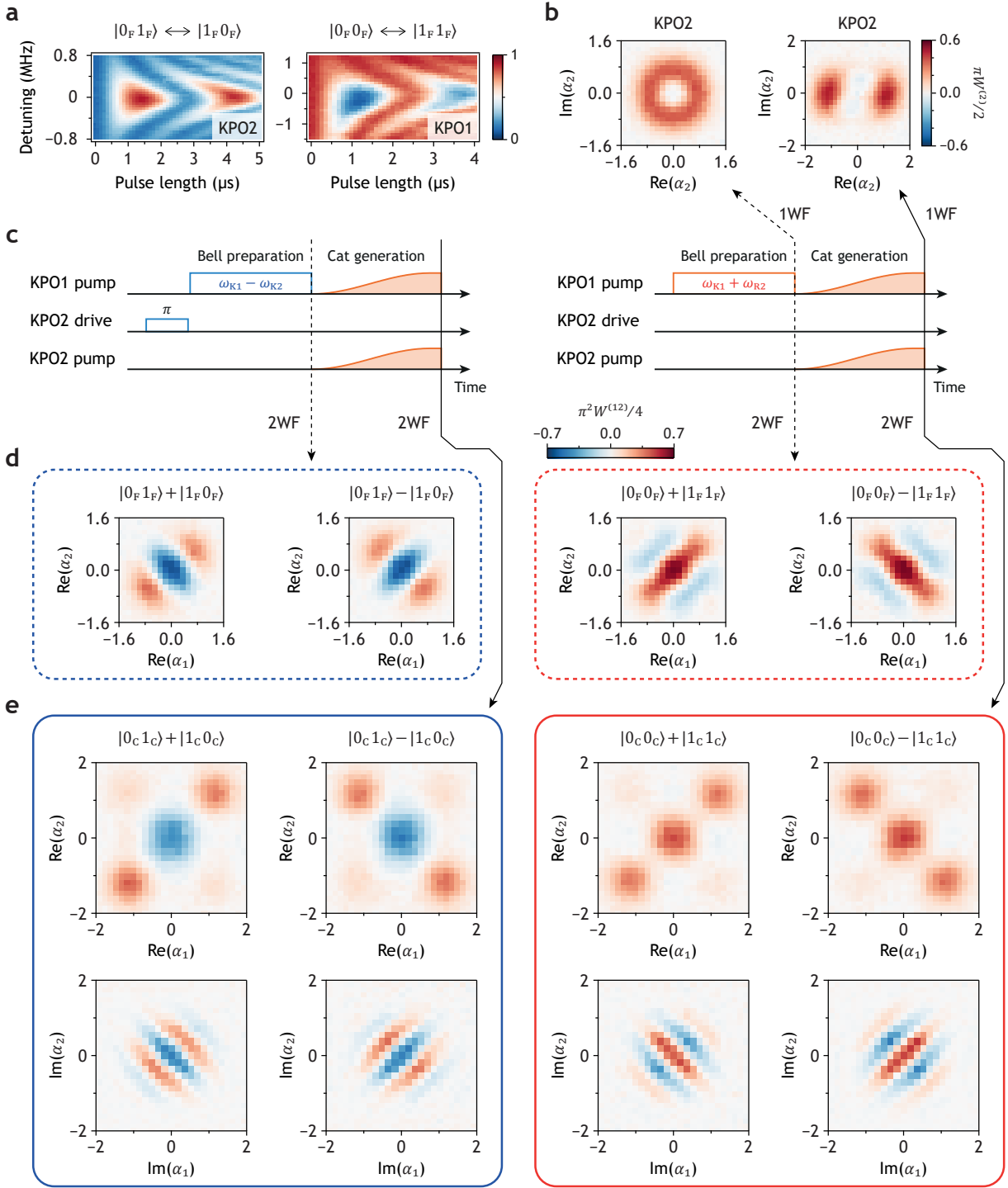


Fig. 2: Converting Bell-Fock states to Bell-Cat states. **a** Rabi oscillations for Bell-preparation pulse. Regarding Rabi oscillations associated with $|0_F 1_F\rangle \leftrightarrow |1_F 0_F\rangle$ transitions, the colour represents the population of the $|0_F\rangle$ state of KPO2 and zero detuning corresponds to the frequency $\omega_{K1} - \omega_{K2}$. As for Rabi oscillations associated with $|0_F 0_F\rangle \leftrightarrow |1_F 1_F\rangle$ transitions, the colour represents the population of the $|0_F\rangle$ state of KPO1 and zero detuning corresponds to the frequency $\omega_{K1} + \omega_{K2} - \Delta_{AC}$, where Δ_{AC} is an AC Stark-like frequency shift whose value is 21 MHz in this measurement. **b** Measured one-mode Wigner function (1WF) of Bell-Fock and Bell-Cat states. **c** Pulse sequences for Bell-Fock state preparation and Bell-Cat state generation. The amplitude and length of pulses are not to scale. **d,e** Measured two-mode Wigner function (2WF) for Bell-Fock (d) and Bell-Cat (e) states. In Re-Re plots, $\text{Im}(\alpha_1) = \text{Im}(\alpha_2) = 0$, whereas in Im-Im plots, $\text{Re}(\alpha_1) = \text{Re}(\alpha_2) = 0$. The colour represents the joint number parity.

2WFs for the target states are shown in Supplementary Fig. 3.) The primary sources of this difference are thermal excitation and relaxations, such as single-photon loss and dephasing [45, 54]. Thermal excitation sets an upper limit on fidelity: if we start from a thermal state rather than a vacuum state, the fidelity is inherently limited, even in the absence of relaxations and with perfect control. In our case, this upper bound is 0.86, which is the fidelity between the vacuum state and the tensor-product thermal states of both KPOs.

Approximately 0.13 of the fidelity is lost due to relaxations, based on simulations of our Bell–Fock state preparation and cat generation using the Lindblad master equation. For the cat generation process, dephasing is not considered because low-frequency noise does not affect the fidelity; the cat states in KPOs are protected by the energy gap [24, 55]. Experimental evidence suggests that the primary source of relaxation for cat states in a KPO is single-photon loss [29, 34, 56].

Assuming $T_1 = T_2 = 100$ μ s [57–60] and a thermal photon number of 0.01, the fidelity of the Bell–Fock states is approximately 0.96, while the Bell–Cat state fidelity can reach about 0.93, as simulated by the Lindblad master equation. The main source of remaining infidelity arises from population leakage from the computational subspace due to the small Kerr coefficient. This issue can be mitigated by using a counterdiabatic or numerically optimized pulse [28, 61, 62]. (In this work, a counterdiabatic pulse was not used, unlike in our previous work [29]. See Methods for more information.)

The final fidelity from the simulation, accounting for all these error sources, is approximately 0.68, which is reasonably close to our experimental result. For more details on the simulation, see Sec. 4A of Supplementary Information.

C. Two-cat gate operation

One notable feature of this KPO system is that the same type of parametric pulse can be used for two-qubit gate operations in both Fock- and cat-state encodings [49]. In this work, a parametric pulse—referred to as the gate pulse—with a frequency of $(\omega_{p1} - \omega_{p2})/2$ was employed for the gate operation. If $\Delta_1 = \Delta_2$ in Eq. (1), the gate pulse frequency matches that used to prepare the Bell–Fock state. Thus, the schemes for creating Bell–Fock and Bell–Cat states are quite similar, with one key difference: the gate pulse at $(\omega_{p1} - \omega_{p2})/2$ induces not only $|0_{C1C}\rangle \leftrightarrow |1_{C0C}\rangle$ transitions but also $|0_{C0C}\rangle \leftrightarrow |1_{C1C}\rangle$ transitions, the latter of which are forbidden in the Fock-state basis but enabled by the presence of the pump.

Below, we explicitly outline the three-wave mixing processes that facilitate this gate operation. Each term represents the frequency of a photon created or annihilated during the process; for example, ω_{p2} corresponds to the pump for KPO2 and $(\omega_{p1} - \omega_{p2})/2$ to

the gate pulse.

The $|0_{C1C}\rangle \leftrightarrow |1_{C0C}\rangle$ transitions:

$$(i) \omega_{p2} \rightarrow \frac{\omega_{p2}}{2} + \frac{\omega_{p2}}{2}, \quad (ii) \frac{\omega_{p2}}{2} + \frac{\omega_{p1} - \omega_{p2}}{2} \rightarrow \frac{\omega_{p1}}{2}.$$

The $|0_{C0C}\rangle \leftrightarrow |1_{C1C}\rangle$ transitions:

$$(i) \omega_{p2} + \frac{\omega_{p1} - \omega_{p2}}{2} \rightarrow \frac{\omega_{p1} + \omega_{p2}}{2}, \quad (ii) \frac{\omega_{p1} + \omega_{p2}}{2} \rightarrow \frac{\omega_{p1}}{2} + \frac{\omega_{p2}}{2}.$$

Here, the processes (i) and (ii) occur sequentially.

Based on the three-wave mixing processes described above, particularly process (ii), the working principle of our two-cat gate operation can be understood as follows. We begin with the X gate, which can be implemented using a single-photon drive with the frequency $\omega_{p1}/2$ or $\omega_{p2}/2$ [29], as the X gate changes the parity of the state and the cat states are already shaped by the interplay between the Kerr nonlinearity and the two-photon pump. In our two-cat gate, the gate pulse enables the two KPOs to exchange a single photon (for the $|0_{C1C}\rangle \leftrightarrow |1_{C0C}\rangle$ transitions) or absorb/emit a single photon simultaneously (for the $|0_{C0C}\rangle \leftrightarrow |1_{C1C}\rangle$ transitions). Such processes result in two correlated X gates acting on each KPO, implementing the following gate operation \hat{U}_G :

$$\hat{U}_G = \frac{1}{\sqrt{2}} \begin{pmatrix} 1 & 0 & 0 & i \\ 0 & 1 & i & 0 \\ 0 & i & 1 & 0 \\ i & 0 & 0 & 1 \end{pmatrix}. \quad (2)$$

Within the $|0_{C1C}\rangle$ and $|1_{C0C}\rangle$ subspace, the gate operation remains identical to the \sqrt{iSWAP} gate. For simplicity, we refer to it as the \sqrt{iSWAP} gate in this work. (This work does not explore $|0_{C0C}\rangle \leftrightarrow |1_{C1C}\rangle$ transitions. A complete characterization of the gate operation, including this aspect, is left for future study.)

Note that Eq. (2) corresponds to the \hat{R}_{ZZ} gate in the coherent-state basis (see Sec. 6 of the Supplementary Information for the derivation). This has two key implications: Since the \hat{R}_{ZZ} gate is part of the universal gate set, Eq. (2) is as well. Additionally, the \hat{R}_{ZZ} gate—and therefore Eq. (2)—preserves the biased-noise property of KPOs, as discussed in Ref. [33].

We observe the Rabi-like oscillations in the parity of each KPO, which we call the two-cat Rabi, as a function of the phase and the detuning of the parametric pulse (Fig. 3a,b). Here, the gate phase ϕ_g is the phase relative to the pumps, and the gate detuning Δ_g is the detuning from $(\omega_{p1} - \omega_{p2})/2$. For this measurement, we first prepare $|0_{F1F}\rangle$ and convert it to $|0_{C1C}\rangle$ by applying the pumps. Then, we apply the gate pulse, in addition to the pumps, as shown in Fig. 3c.

Note that the two KPOs exhibit the same two-cat Rabi oscillations but with opposite parities. From the simulation, we determined the gate amplitude to be 2.96 MHz (see Supplementary Fig. 5a and its caption for details). One-mode Wigner functions show that during the Rabi oscillations, the state evolves from $|0_{C1C}\rangle$ (no gate) to $|1_{C0C}\rangle$ (iSWAP). To determine the intermediate quantum state between these

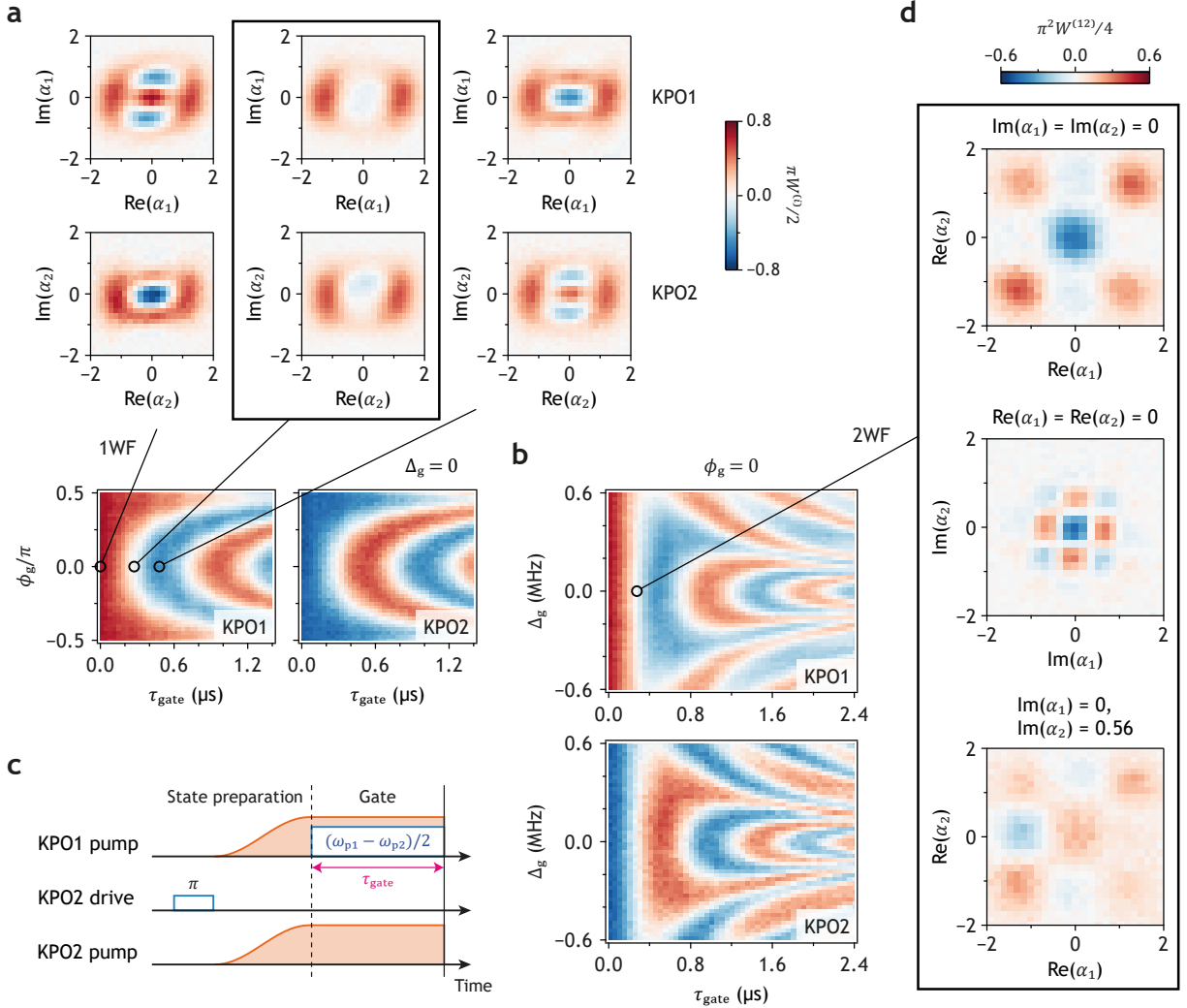


Fig. 3: Two-cat gate operation. **a,b** Two-cat Rabi oscillations between $|0_C1_C\rangle$ and $|1_C0_C\rangle$. The colours represent the number parity of each KPO. ϕ_g and Δ_g represent the phase and detuning of the gate pulse, respectively. Zero detuning ($\Delta_g = 0$) means that the frequency of the gate pulse is equal to $(\omega_{p1} - \omega_{p2})/2$. One-mode Wigner functions at times corresponding to no gate (0 ns), $\sqrt{i\text{SWAP}}$ gate (275 ns), and $i\text{SWAP}$ gate (480 ns) are shown above. **c** Pulse sequence for the two-cat Rabi. **d** Two-mode Wigner functions of the KPO state after the $\sqrt{i\text{SWAP}}$ gate. All Wigner functions showing the results of the $\sqrt{i\text{SWAP}}$ gate are enclosed in black frames.

two points, a 2WF measurement with an additional offset in displacement is required. This is because 1WF and the Re-Re (Im-Im) plot in 2WF without an additional displacement along the imaginary (real) axes cannot distinguish the following three states: $|0_C1_C\rangle \pm i|1_C0_C\rangle$, which are the states after the $\sqrt{i\text{SWAP}}$ gate, and the mixture of $|0_C1_C\rangle$ and $|1_C0_C\rangle$. The Re-Re plot with an additional offset shows that the state is $|0_C1_C\rangle - i|1_C0_C\rangle$ (the plot at the bottom of Fig. 3d), confirming that the two-cat gate operation is the $\sqrt{i\text{SWAP}}$ gate (see Supplementary Fig. 3).

The $\sqrt{i\text{SWAP}}$ gate time, 275 ns, is significantly faster than recent implementations of similar SWAP gate operations on bosonic modes [50, 51]. This short gate time is possible because the beam-splitter interaction is inherently built into the Hamiltonian [Eq. (1)], and the KPO system enables us to adopt

schemes for gate operations in Fock-state encoding. The primary limitations on our gate time are the AC Stark-like frequency shift induced by the gate pulse above a certain amplitude threshold, which would introduce unwanted Z-gate operations, and the small cat size. Additionally, Ref. [49] suggested implementing Eq. (2) using the frequency $(\omega_{p1} + \omega_{p2})/2$, as we demonstrated in Fig. 2 for the preparation of Bell-Fock states. We did not pursue this approach because the amplitude threshold for the AC Stark-like frequency shift is almost zero at $(\omega_{p1} + \omega_{p2})/2$. Therefore, suppressing the AC Stark-like frequency shift at the circuit design level and increasing the cat size will enable faster gate operations and enhance functionalities.

Similarly to the Bell-Fock state preparation, the sign of the superposition can be flipped by adding π in the phase of the two-cat gate pulse. Unlike the con-

version from the Bell–Fock to Bell–Cat states, however, we cannot create a Bell–Cat state with an arbitrary phase. The reason is that once the pumps are turned on, the pump phase becomes the reference phase. Consequently, we can no longer use the virtual Z gate as implied in Fig. 3a. In other words, ϕ_d in $|0_F1_F\rangle + e^{i\phi_d}|1_F0_F\rangle$ can only take values of $(n+1/2)\pi$, where n is an integer. Thus, the Bell–Cat state we create in this work using the two-cat gate is limited to $|0_C1_C\rangle \pm i|1_C0_C\rangle$, which is exactly what is expected from the $\sqrt{i\text{SWAP}}$ gate.

The gate-detuning dependence of the two-cat Rabi exhibits the characteristic pattern observed in cat Rabi oscillations for the X gate [29]. This suggests that, as pointed out in Ref. [29], when mapping the dynamics of cat states to that of interacting two-level qubits, two tones with opposite gate detuning are required. In such a two-level qubit system, the same pattern can be reproduced by modulating the coupling constant with two frequencies, ω_g and $2(\omega_{q1} - \omega_{q2}) - \omega_g$, where ω_{qi} is the transition frequency of the two-level qubit i ($i = 1, 2$). In this case, zero detuning corresponds to $\omega_g = \omega_{q1} - \omega_{q2}$. For further discussion and simulation results, see Sec. 5 of Supplementary Information.

The fidelity of the $|0_C1_C\rangle \pm i|1_C0_C\rangle$ states is 0.61 ± 0.03 , which is almost identical to that achieved by the conversion from Bell–Fock to Bell–Cat states. This result is not surprising because, although the pulse length of the $\sqrt{i\text{SWAP}}$ gate on the cat states (275 ns) is less than half that of the Bell-preparation pulse (730 ns), the contrast of the two-cat Rabi oscillations attenuates faster than that of the Rabi oscillations used for the Bell–Fock state preparation (compare Fig. 3b and the left plot of Fig. 2a). More quantitatively, the decay time of the two-cat Rabi oscillation is 3 μs for both KPOs, whereas that of the Rabi oscillations used in Bell–Fock state preparation is longer than 10 μs . The simulation using the Lindblad master equation suggests that the photon lifetime of both KPOs to reproduce the data in Fig. 3b is 10 μs (see Supplementary Fig. 5a). This photon lifetime falls within the observed range (Supplementary Table 1). Thus, the main sources of infidelity in this case are also thermal excitation and relaxations.

The fidelity of our Bell–Cat states is somewhat lower than that reported in previous works, which was 0.74 [50, 51]. This difference is likely due to the low thermal population ($\lesssim 0.01$) in the earlier studies. In fact, the 0.13 difference in fidelity between our work and previous studies closely matches the infidelity attributed to thermal excitation, as discussed in Sec. II B. We expect the performance of our gate operation to be comparable to that of previous demonstrations.

Overall, our gate operation is faster and significantly simpler, requiring only a single square pulse to implement the $\sqrt{i\text{SWAP}}$ gate, while achieving comparable performance. Furthermore, there is considerable potential for improving fidelity by suppressing the thermal population, enhancing the relaxation times of

KPOs, or optimizing the gate pulse shape.

Lastly, we point out that the same $\sqrt{i\text{SWAP}}$ gate operation can be performed between cat states with different mean photon numbers. This property may provide significant flexibility when constructing a KPO-based quantum network, particularly for the scheme developed in Refs. [63, 64]. The simulation results can be found in Supplementary Fig. 5c.

III. DISCUSSION

To summarize, we demonstrate two intuitive methods for entangling cat states by adopting a DV–CV hybrid approach. This hybridization is achieved through Hamiltonian engineering, combining moderate Kerr nonlinearity and two-photon pumping. It enables coherent treatment of Bell–Fock and Bell–Cat states, facilitating gate operations directly on the cat basis without the need for ancilla qubits or individual Fock state control. One consequence is the entanglement-preserving conversion from Bell–Fock to Bell–Cat states. The other is the fast and simple $\sqrt{i\text{SWAP}}$ gate operation on the cat states, thereby completing the demonstration of a universal quantum gate set. Therefore, our superconducting planar KPO system is not only a promising quantum information processing unit but also a potent platform for DV–CV hybridization.

We suggest several future research directions extending this work. First, we can construct quantum networks in the cat basis. Note that our methods are compatible with previously demonstrated quantum network constructions in the Fock basis [63–65]. This means we can create more complex entangled states, such as Greenberger–Horne–Zeilinger or cluster states, in the cat basis simply by replacing transmon/Xmon qubits with KPOs and converting the basis from Fock to cat states. This approach will significantly reduce the complexity of constructing quantum networks using bosonic modes. We can also create travelling entangled-cat states by coupling our system to transmission lines [62]. Combining Hamiltonian engineering with dissipation engineering may enable us to create highly coherent cat states [66–69]. Finally, employing other multiphoton pumps may open new possibilities [70–82], such as exploring condensed matter physics in time crystals [83–85] and autonomous quantum error correction [86].

IV. METHODS

A. Cat state generation

As mentioned in the main text, the ramping time of the pump for cat-state generation is 1 μs . This ramping time is much longer than that in our previous work (300 ns) [29] because the counterdiabatic pulse did not work. We believe that the reason is the

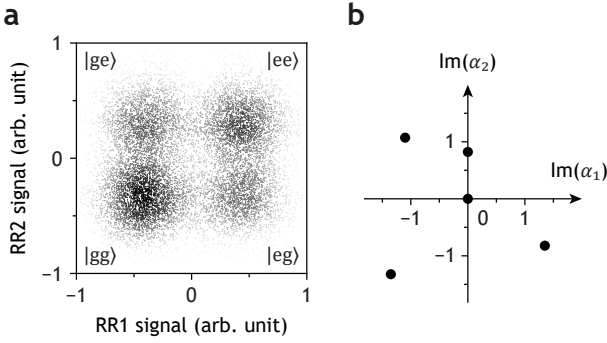


Fig. 4: Configurations for measuring two-mode Wigner functions. **a** Typical single-shot results. RR stands for “readout resonator”. **b** Coordinates of offset displacement for Re–Re plots of a two-mode Wigner function.

reduction in Kerr coefficient from about 3 MHz to 2 MHz after ramping up the pump (see Supplementary Table 1), whereas the Kerr coefficient in Ref. [29] increases slightly from 2.86 MHz to 3.13 MHz.

During the ramping, we change the pump frequency, i.e., chirp the pump pulse, for two reasons: One is to compensate for unwanted AC Stark-like frequency shifts in $2\omega_{K1}$ and $2\omega_{K2}$, which are approximately -10 MHz at the target pump amplitude [29]. The other reason is that the pump detuning must start from zero and then approach the target value adiabatically to create high-fidelity cat states.

B. Wigner-function measurements

The one-mode Wigner function of the KPO is given by [87]

$$W^{(i)}(\alpha_i) = \frac{2}{\pi} \text{Tr} \left[\hat{D}^\dagger(\alpha_i) \rho^{(i)} \hat{D}(\alpha_i) \hat{\Pi}^{(i)} \right], \quad (3)$$

where $\hat{D}(\alpha_i) = \exp(\alpha_i \hat{a}_i^\dagger - \alpha_i^* \hat{a}_i)$ is the displacement operator, $\hat{\Pi}^{(i)} = \exp(i\pi \hat{a}_i^\dagger \hat{a}_i)$ is the photon-number parity operator, and $\rho^{(i)}$ is the density matrix of KPO*i* ($i = 1, 2$). Similarly, the two-mode Wigner function is given by [45]

$$W^{(12)}(\alpha_1, \alpha_2) = \frac{4}{\pi^2} \text{Tr} \left[\hat{D}^\dagger(\alpha_2) \hat{D}^\dagger(\alpha_1) \rho^{(12)} \hat{D}(\alpha_1) \hat{D}(\alpha_2) \hat{\Pi}^{(12)} \right] \quad (4)$$

$$= \frac{4}{\pi^2} \langle \hat{\Pi}^{(12)}(\alpha_1, \alpha_2) \rangle, \quad (5)$$

where $\rho^{(12)}$ is the density matrix of the two-KPO system and $\hat{\Pi}^{(12)} = \hat{\Pi}^{(1)} \hat{\Pi}^{(2)}$ is the joint parity of the two KPOs. This operator can be measured by the joint probabilities of the transmons being in their ground/excited state P_{jk} ($j, k \in \{g, e\}$) [53]:

$$\langle \hat{\Pi}^{(12)}(\alpha_1, \alpha_2) \rangle = P_{ee} + P_{gg} - P_{eg} - P_{ge}. \quad (6)$$

In the experiment, this was accomplished by fitting the single-shot readout data (Fig. 4a) with a two-dimensional Gaussian function for all pixels of the Wigner function plots.

The two-mode Wigner functions of the target and simulated states in Supplementary Information are obtained using the Cahill–Glauber formula [88–90]:

$$W^{(12)}(\alpha_1, \alpha_2) = \frac{4}{\pi^2} \text{Tr} \left[\rho^{(12)} \hat{T}(\alpha_1) \hat{T}(\alpha_2) \right] \quad (7)$$

$$= \frac{4}{\pi^2} \sum_{\{n_i\}=0}^{N_i} \sum_{\{m_i\}=0}^{N_i} \prod_{i=1}^2 \langle n_i | \hat{T}(\alpha_i) | m_i \rangle \times \langle \{m_i\} | \rho^{(12)} | \{n_i\} \rangle, \quad (8)$$

where \hat{T} is the complex Fourier transform of the displacement operator, and N_i is the dimension of the Hilbert space of KPO*i*. For $m_i \geq n_i$,

$$\langle n_i | \hat{T}(\alpha_i) | m_i \rangle = \sqrt{\frac{n_i!}{m_i!}} (-1)^{n_i} (2\alpha_i^*)^{\delta_i} \times L_{n_i}^{(\delta_i)}(4|\alpha_i|^2) \exp(-2|\alpha_i|^2), \quad (9)$$

where $\delta_i \equiv m_i - n_i$ and $L_{n_i}^{(\delta_i)}(x)$ are the associated Laguerre polynomials. For $m_i < n_i$, we can use the following property:

$$\langle n_i | \hat{T}(\alpha_i) | m_i \rangle = \langle m_i | \hat{T}(\alpha_i^*) | n_i \rangle. \quad (10)$$

C. Density-matrix reconstruction

A two-mode Wigner function is a four-dimensional function. Since our signal-to-noise ratio is marginal, as shown in Fig. 4a, collecting such a large data set— $13 \times 13 \times 13 \times 13$ pixels, for example—is impractical. Instead, we measured 10 two-dimensional plots, each of which has 17×17 pixels in the range $-1.6 \leq \alpha_i \leq 1.6$ ($i = 1, 2$). Among these 10 plots, half are Re–Re plots with imaginary offset displacements and the other half are Im–Im plots with real offset displacements. For Re–Re plots, the imaginary offset displacements are given as follows (Fig. 4b): $\{(\text{Im}(\alpha_1), \text{Im}(\alpha_2))\} = \{(0, 0), (0, +0.82), (-1.10, +1.07), (-1.35, -1.32), (+1.35, -0.82)\}$. The same values are used for the real offset displacements for Im–Im plots. In addition to the 10 plots from the two-mode Wigner function, one-mode Wigner functions of both KPOs were measured, resulting in a total of 12 plots used for density matrix reconstruction.

We found that, with the data set simulated from the target Bell–Cat states, the reconstruction fidelity is >0.99 . We also checked the reconstruction fidelity of non-ideal data sets. For example, we prepared low-quality Bell–Cat states by simulating the Lindblad master equation with $T_1 = 10$ μ s for both KPOs after 2 μ s waiting; the resulting fidelity between this state and the initial state was 0.57, which is similar

to our results. The reconstruction fidelity from 2WFs of these low-quality states is still ≥ 0.98 .

For Bell–Fock states, the dimensions of the Hilbert space were set to 3×3 . For Bell–Cat states, the dimensions of the Hilbert space were set to 8×8 because, for the ideal Bell–Cat states with $P/K = 1$ and 1 MHz of pump detuning, the occupation probability at $|\geq 8\rangle$ is less than 10^{-4} .

The algorithm for reconstruction followed the idea from Refs. [91, 92], which use gradient descent to reconstruct a density matrix with a projection step. A loss function between the measured data and that obtained from an estimated density matrix is minimized to obtain the reconstructed density matrix starting from a random initialization. We simplified the method to directly apply gradient descent (Adam [93]) on a matrix T , that is projected to construct an estimate of the physical density matrix using the Cholesky decomposition. At each gradient-descent step, the loss function is minimized followed by a projection step where the matrix T is converted to a lower triangular matrix with real-valued diagonal elements by discarding the upper-triangular part and making the diagonal real. This step allows us to obtain a density matrix $\rho = \frac{T^\dagger T}{\text{Tr}(T^\dagger T)}$ that is guaranteed to be physical. The Python libraries used were QuTiP [94, 95], NumPy [96], and JAX [97].

Data availability: All data are available in the main text or in the supplementary information.

REFERENCES

- [1] L. M. K. Vandersypen and I. L. Chuang, *NMR techniques for quantum control and computation*, Rev. Mod. Phys. **76**, 1037 (2005).
- [2] P. Krantz, M. Kjaergaard, F. Yan, T. P. Orlando, S. Gustavsson, and W. D. Oliver, *A quantum engineer’s guide to superconducting qubits*, Appl. Phys. Rev. **6**, 021318 (2019).
- [3] S. Kwon, A. Tomonaga, G. L. Bhai, S. J. Devitt, and J.-S. Tsai, *Gate-based superconducting quantum computing*, J. Appl. Phys. **129**, 041102 (2021).
- [4] G. Burkard, T. D. Ladd, A. Pan, J. M. Nichol, and J. R. Petta, *Semiconductor spin qubits*, Rev. Mod. Phys. **95**, 025003 (2023).
- [5] S. L. Braunstein and P. van Loock, *Quantum information with continuous variables*, Rev. Mod. Phys. **77**, 513 (2005).
- [6] A. Joshi, K. Noh, and Y. Y. Gao, *Quantum information processing with bosonic qubits in circuit QED*, Quantum Sci. Technol. **6**, 033001 (2021).
- [7] A. M. Eriksson, T. Sépulcre, M. Kervinen, T. Hillmann, M. Kudra, S. Dupouy, Y. Lu, M. Khanahmadi, J. Yang, C. Castillo-Moreno, P. Delsing, and S. Gasparinetti, *Universal control of a bosonic mode via drive-activated native cubic interactions*, Nat. Commun. **15**, 2512 (2024).
- [8] U. L. Andersen, J. S. Neergaard-Nielsen, P. van Loock, and A. Furusawa, *Hybrid discrete- and continuous-variable quantum information*, Nature Phys. **11**, 713–719 (2015).
- [9] H. Jeong, A. Zavatta, M. Kang, S.-W. Lee, L. S. Costanzo, S. Grandi, T. C. Ralph, and M. Bellini, *Generation of hybrid entanglement of light*, Nature Photon. **8**, 564–569 (2014).
- [10] O. Morin, K. Huang, J. Liu, H. Le Jeannic, C. Fabre, and J. Laurat, *Remote creation of hybrid entanglement between particle-like and wave-like optical qubits*, Nature Photon. **8**, 570–574 (2014).
- [11] A. E. Ulanov, D. Sychev, A. A. Pushkina, I. A. Fedorov, and A. I. Lvovsky, *Quantum Teleportation Between Discrete and Continuous Encodings of an Optical Qubit*, Phys. Rev. Lett. **118**, 160501 (2017).
- [12] D. V. Sychev, A. E. Ulanov, E. S. Tiunov, A. A. Pushkina, A. Kuzhamuratov, V. Novikov, and A. I. Lvovsky, *Entanglement and teleportation between polarization and wave-like encodings of an optical qubit*, Nat. Commun. **9**, 3672 (2018).
- [13] H. C. J. Gan, G. Maslennikov, K.-W. Tseng, C. Nguyen, and D. Matsukevich, *Hybrid Quantum Computing with Conditional Beam Splitter Gate in Trapped Ion System*, Phys. Rev. Lett. **124**, 170502 (2020).
- [14] T. Darras, B. E. Asenbeck, G. Guccione, A. Cavaillès, H. Le Jeannic, and J. Laurat, *A quantum-bit encoding converter*, Nat. Photon. **17**, 165–170 (2023).
- [15] A. Macridin, A. C. Y. Li, and P. Spentzouris, *Qumode transfer between continuous- and discrete-variable devices*, Phys. Rev. A **109**, 032419 (2024).
- [16] M. Dykman, in *Fluctuating Nonlinear Oscillators: From Nanomechanics to Quantum Superconducting Circuits*, edited by M. Dykman (Oxford University Press, 2012).
- [17] H. Goto, *Quantum computation based on quantum adiabatic bifurcations of Kerr-nonlinear parametric oscillators*, J. Phys. Soc. Jpn. **88**, 061015 (2019).
- [18] W. Wustmann and V. Shumeiko, *Parametric effects in circuit quantum electrodynamics*, Low Temp. Phys. **45**, 848–869 (2019).
- [19] T. Yamaji, S. Kagami, A. Yamaguchi, T. Satoh, K. Koshino, H. Goto, Z. R. Lin, Y. Nakamura, and T. Yamamoto, *Spectroscopic observation of the crossover from a classical Duffing oscillator to a Kerr parametric oscillator*, Phys. Rev. A **105**, 023519 (2022).
- [20] A. Yamaguchi, S. Masuda, Y. Matsuzaki, T. Yamaji, T. Satoh, A. Morioka, Y. Kawakami, Y. Igarashi, M. Shirane, and T. Yamamoto, *Spectroscopy of flux-driven Kerr parametric oscillators by reflection coefficient measurement*, New. J. Phys. **26**, 043019 (2024).
- [21] P. T. Cochrane, G. J. Milburn, and W. J. Munro, *Macroscopically distinct quantum-superposition states as a bosonic code for amplitude damping*, Phys. Rev. A **59**, 2631–2634 (1999).
- [22] H. Goto, *Bifurcation-based adiabatic quantum computation with a nonlinear oscillator network*, Sci. Rep. **6**, 21686 (2016).

[23] F. Minganti, N. Bartolo, J. Lolli, W. Casteels, and C. Ciuti, *Exact results for Schrödinger cats in driven-dissipative systems and their feedback control*, Sci. Rep. **6**, 26987 (2016).

[24] S. Puri, S. Boutin, and A. Blais, *Engineering the quantum states of light in a Kerr-nonlinear resonator by two-photon driving*, npj Quantum Inf. **3**, 18 (2017).

[25] Y. Zhang and M. I. Dykman, *Preparing quasienergy states on demand: A parametric oscillator*, Phys. Rev. A **95**, 053841 (2017).

[26] Z. Wang, M. Pechal, E. A. Wollack, P. Arrangoiz-Arriola, M. Gao, N. R. Lee, and A. H. Safavi-Naeini, *Quantum dynamics of a few-photon parametric oscillator*, Phys. Rev. X **9**, 021049 (2019).

[27] S. Masuda, T. Ishikawa, Y. Matsuzaki, and S. Kawabata, *Controls of a superconducting quantum parametron under a strong pump field*, Sci. Rep. **11**, 11459 (2021).

[28] J.-J. Xue, K.-H. Yu, W.-X. Liu, X. Wang, and H.-R. Li, *Fast generation of cat states in Kerr nonlinear resonators via optimal adiabatic control*, New J. Phys. **24**, 053015 (2022).

[29] D. Iyama, T. Kamiya, S. Fujii, H. Mukai, Y. Zhou, T. Nagase, A. Tomonaga, R. Wang, J.-J. Xue, S. Watabe, S. Kwon, and J.-S. Tsai, *Observation and manipulation of quantum interference in a superconducting Kerr parametric oscillator*, Nat. Commun. **15**, 86 (2024).

[30] M. Marthaler and M. I. Dykman, *Quantum interference in the classically forbidden region: A parametric oscillator*, Phys. Rev. A **76**, 010102(R) (2007).

[31] J. Venkatraman, R. G. Cortinas, N. E. Frattini, X. Xiao, and M. H. Devoret, *A driven Kerr oscillator with two-fold degeneracies for qubit protection*, Proc. Natl. Acad. Sci. U.S.A. **121**, e2311241121 (2024).

[32] H. Goto, *Universal quantum computation with a nonlinear oscillator network*, Phys. Rev. A **93**, 050301(R) (2016).

[33] S. Puri, L. St-Jean, J. A. Gross, A. Grimm, N. E. Frattini, P. S. Iyer, A. Krishna, S. Touzard, L. Jiang, A. Blais, S. T. Flammia, and S. M. Girvin, *Bias-preserving gates with stabilized cat qubits*, Sci. Adv. **6**, eaay5901 (2020).

[34] A. Grimm, N. E. Frattini, S. Puri, S. O. Mundhada, S. Touzard, M. Mirrahimi, S. M. Girvin, S. Shankar, and M. H. Devoret, *Stabilization and operation of a Kerr-cat qubit*, Nature **584**, 205 (2020).

[35] T. Kanao, S. Masuda, S. Kawabata, and H. Goto, *Quantum gate for Kerr-nonlinear parametric oscillator using effective excited states*, Phys. Rev. Applied **18**, 014019 (2022).

[36] Q. Xu, J. K. Iverson, F. G. S. L. Brandão, and L. Jiang, *Engineering fast bias-preserving gates on stabilized cat qubits*, Phys. Rev. Research **4**, 013082 (2022).

[37] S. Masuda, T. Kanao, H. Goto, Y. Matsuzaki, T. Ishikawa, and S. Kawabata, *Fast Tunable Coupling Scheme of Kerr Parametric Oscillators Based on Shortcuts to Adiabaticity*, Phys. Rev. Applied **18**, 034076 (2022).

[38] A. Hajr, B. Qing, K. Wang, G. Koolstra, Z. Pedramrazi, Z. Kang, L. Chen, L. B. Nguyen, C. Jünger, N. Goss, I. Huang, B. Bhandari, N. E. Frattini, S. Puri, J. Dressel, A. N. Jordan, D. I. Santiago, and I. Siddiqi, *High-Coherence Kerr-Cat Qubit in 2D Architecture*, Phys. Rev. X **14**, 041049 (2024).

[39] T. Yamaji, S. Masuda, A. Yamaguchi, T. Satoh, A. Morioka, Y. Igarashi, M. Shirane, and T. Yamamoto, *Correlated Oscillations in Kerr Parametric Oscillators with Tunable Effective Coupling*, Phys. Rev. Applied **20**, 014057 (2023).

[40] G. Margiani, J. del Pino, T. L. Heugel, N. E. Bousse, S. Guerrero, T. W. Kenny, O. Zilberberg, D. Sabonis, and A. Eichler, *Deterministic and stochastic sampling of two coupled Kerr parametric oscillators*, Phys. Rev. Research **5**, L012029 (2023).

[41] P. Álvarez, D. Pittilini, F. Misericocchi, S. Raamamurthy, G. Margiani, O. Ameye, J. del Pino, O. Zilberberg, and A. Eichler, *Biased Ising Model Using Two Coupled Kerr Parametric Oscillators with External Force*, Phys. Rev. Lett. **132**, 207401 (2024).

[42] F. Dell'Anno, S. De Siena, and F. Illuminati, *Multi-photon quantum optics and quantum state engineering*, Phys. Rep. **428**, 53-168 (2006).

[43] B. C. Sanders, *Review of entangled coherent states*, J. Phys. A: Math. Theor. **45**, 244002 (2012).

[44] M. Walschaers, *Non-Gaussian Quantum States and Where to Find Them*, PRX Quantum **2**, 030204 (2021).

[45] C. Wang, Y. Y. Gao, P. Reinhold, R. W. Heeres, N. Ofek, K. Chou, C. Axline, M. Reagor, J. Blumoff, K. M. Sliwa, L. Frunzio, S. M. Girvin, L. Jiang, M. Mirrahimi, M. H. Devoret, and R. J. Schoelkopf, *A Schrödinger Cat Living in Two Boxes*, Science **352**, 1087-1091 (2016).

[46] V. V. Albert, S. O. Mundhada, A. Grimm, S. Touzard, M. H. Devoret, and L. Jiang, *Pair-cat codes: autonomous error-correction with low-order nonlinearity*, Quantum Sci. Technol. **4**, 035007 (2019).

[47] Z.-Y. Zhou, C. Gneiting, J. Q. You, and F. Nori, *Generating and detecting entangled cat states in dissipatively coupled degenerate optical parametric oscillators*, Phys. Rev. A **104**, 013715 (2021).

[48] J. M. Gertler, S. van Geldern, S. Shirol, L. Jiang, and C. Wang, *Experimental Realization and Characterization of Stabilized Pair-Coherent States*, PRX Quantum **4**, 020319 (2023).

[49] H. Chono, T. Kanao, and H. Goto, *Two-qubit gate using conditional driving for highly detuned Kerr nonlinear parametric oscillators*, Phys. Rev. Research **4**, 043054 (2022).

[50] Y. Y. Gao, B. J. Lester, K. S. Chou, L. Frunzio, M. H. Devoret, L. Jiang, S. M. Girvin, and R. J. Schoelkopf, *Entanglement of bosonic modes through an engineered exchange interaction*, Nature **566**, 509 (2019).

[51] B. J. Chapman, S. J. de Graaf, S. H. Xue, Y. Zhang, J. Teoh, J. C. Curtis, T. Tsunoda, A. Eickbusch, A. P. Read, A. Koottandavida, S. O. Mundhada, L. Frunzio, M. H. Devoret, S. M. Girvin, and R. J. Schoelkopf, *High-On-Off-Ratio Beam-Splitter Inter-*

action for Gates on Bosonically Encoded Qubits, PRX Quantum **4**, 020355 (2023).

[52] M. B. Plenio and S. S. Virmani, *An Introduction to Entanglement Theory in Quantum Information and Coherence*, edited by E. Andersson and P. Öhberg (Springer Cham, 2014); https://doi.org/10.1007/978-3-319-04063-9_8

[53] M. S. Kim and J. Lee, *Test of quantum nonlocality for cavity fields*, Phys. Rev. A **61**, 042102 (2000).

[54] X. L. Zhao, Z. C. Shi, M. Qin, and X. X. Yi, *Optical Schrödinger cat states in one mode and two coupled modes subject to environments*, Phys. Rev. A **96**, 013824 (2017).

[55] S. Puri, A. Grimm, P. Campagne-Ibarcq, A. Eickbusch, K. Noh, G. Roberts, L. Jiang, M. Mirrahimi, M. H. Devoret, and S. M. Girvin, *Stabilized cat in a driven nonlinear cavity: A fault-tolerant error syndrome detector*, Phys. Rev. X **9**, 041009 (2019).

[56] N. E. Frattini, R. G. Cortiñas, J. Venkatraman, X. Xiao, Q. Su, C. U Lei, B. J. Chapman, V. R. Joshi, S. M. Girvin, R. J. Schoelkopf, S. Puri, and M. H. Devoret, *Observation of Pairwise Level Degeneracies and the Quantum Regime of the Arrhenius Law in a Double-Well Parametric Oscillator*, Phys. Rev. X **14**, 031040 (2024).

[57] A. P. M. Place, L. V. H. Rodgers, P. Mundada, B. M. Smitham, M. Fitzpatrick, Z. Leng, A. Premkumar, J. Bryon, A. Vrajitoarea, S. Sussman, G. Cheng, T. Madhavan, H. K. Babla, X. H. Le, Y. Gang, B. Jäck, A. Gyenis, N. Yao, R. J. Cava, N. P. de Leon, and A. A. Houck, *New material platform for superconducting transmon qubits with coherence times exceeding 0.3 milliseconds*, Nat. Commun. **12**, 1779 (2021).

[58] C. Wang, X. Li, H. Xu, Z. Li, J. Wang, Z. Yang, Z. Mi, X. Liang, T. Su, C. Yang, G. Wang, W. Wang, Y. Li, M. Chen, C. Li, K. Linghu, J. Han, Y. Zhang, Y. Feng, Y. Song, T. Ma, J. Zhang, R. Wang, P. Zhao, W. Liu, G. Xue, Y. Jin, and H. Yu, *Towards practical quantum computers: transmon qubit with a lifetime approaching 0.5 milliseconds*, npj Quantum inf. **8**, 3 (2022).

[59] S. Kono, J. Pan, M. Chegnizadeh, X. Wang, A. Youssefi, M. Scigliuzzo, and T. J. Kippenberg, *Mechanically induced correlated errors on superconducting qubits with relaxation times exceeding 0.4 ms*, Nat. Commun. **15**, 3950 (2024).

[60] J. Biznárová, A. Osman, E. Rehnman, L. Chayanun, C. Križan, P. Malmberg, M. Rommel, C. Warren, P. Delsing, A. Yurgens, J. Bylander, and A. Fadavi Roudsari, *Mitigation of interfacial dielectric loss in aluminum-on-silicon superconducting qubits*, Preprint at <https://doi.org/10.48550/arXiv.2310.06797> (2023).

[61] F. Motzoi, J. M. Gambetta, P. Rebentrost, and F. K. Wilhelm, *Simple Pulses for Elimination of Leakage in Weakly Nonlinear Qubits*, Phys. Rev. Lett. **103**, 110501 (2009).

[62] H. Goto, Z. Lin, T. Yamamoto, and Y. Nakamura, *On-demand generation of traveling cat states using a parametric oscillator*, Phys. Rev. A **99**, 023838 (2019).

[63] Y. Zhong, H.-S. Chang, A. Bienfait, É. Dumur, M.-H. Chou, C. R. Conner, J. Grebel, R. G. Povey, H. Yan, D. I. Schuster, and A. N. Cleland, *Deterministic multi-qubit entanglement in a quantum network*, Nature **590**, 571–575 (2021).

[64] J. Qiu, Y. Liu, J. Niu, L. Hu, Y. Wu, L. Zhang, W. Huang, Y. Chen, J. Li, S. Liu, Y. Zhong, L. Duan, and D. Yu, *Deterministic quantum teleportation between distant superconducting chips*, Preprint at <https://doi.org/10.48550/arXiv.2302.08756> (2023).

[65] P. Kurpiers, P. Magnard, T. Walter, B. Royer, M. Pechal, J. Heinsoo, Y. Salathé, A. Akin, S. Storz, J.-C. Besse, S. Gasparinetti, A. Blais, and A. Wallraff, *Deterministic quantum state transfer and remote entanglement using microwave photons*, Nature **558**, 264–267 (2018).

[66] R. Gautier, A. Sarlette, and M. Mirrahimi, *Combined Dissipative and Hamiltonian Confinement of Cat Qubits*, PRX Quantum **3**, 020339 (2022).

[67] L. Gravina, F. Minganti, and V. Savona, *Critical Schrödinger Cat Qubit*, PRX Quantum **4**, 020337 (2023).

[68] A. Marquet, A. Essig, J. Cohen, N. Cottet, A. Murani, E. Albertinale, S. Dupouy, A. Bienfait, T. Peronnin, S. Jezouin, R. Lescanne, and B. Huard, *Autoparametric Resonance Extending the Bit-Flip Time of a Cat Qubit up to 0.3 s*, Phys. Rev. X **14**, 021019 (2024).

[69] U. Réglade, A. Bocquet, R. Gautier, J. Cohen, A. Marquet, E. Albertinale, N. Pankratova, M. Hallén, F. Rautschke, L.-A. Sellème, P. Rouchon, A. Sarlette, M. Mirrahimi, P. Campagne-Ibarcq, R. Lescanne, S. Jezouin, and Z. Leghtas, *Quantum control of a cat qubit with bit-flip times exceeding ten seconds*, Nature **629**, 778–783 (2024).

[70] I.-M. Svensson, A. Bengtsson, P. Krantz, J. Bylander, V. Shumeiko, and P. Delsing, *Period-tripling subharmonic oscillations in a driven superconducting resonator*, Phys. Rev. B **96**, 174503 (2017).

[71] I.-M. Svensson, A. Bengtsson, J. Bylander, V. Shumeiko, and P. Delsing, *Period multiplication in a parametrically driven superconducting resonator*, Appl. Phys. Lett. **113**, 022602 (2018).

[72] C. W. S. Chang, C. Sabín, P. Forn-Díaz, F. Quijandría, A. M. Vadiraj, I. Nsanzineza, G. Johansson, and C. M. Wilson, *Observation of Three-Photon Spontaneous Parametric Down-Conversion in a Superconducting Parametric Cavity*, Phys. Rev. X **10**, 011011 (2020).

[73] Y. Zhang, J. Gosner, S. M. Girvin, J. Ankerhold, and M. I. Dykman, *Time-translation-symmetry breaking in a driven oscillator: From the quantum coherent to the incoherent regime*, Phys. Rev. A **96**, 052124 (2017).

[74] Y. Zhang and M. I. Dykman, *Nonlocal random walk over Floquet states of a dissipative nonlinear oscillator*, Phys. Rev. E **100**, 052148 (2019).

[75] Y. Tadokoro, H. Tanaka, and M. I. Dykman, *Noise-induced switching from a symmetry-protected shallow metastable state*, Sci. Rep. **10**, 10413 (2020).

[76] J. Gosner, B. Kubala, and J. Ankerhold, *Relaxation*

dynamics and dissipative phase transition in quantum oscillators with period tripling, Phys. Rev. B **101**, 054501 (2020).

[77] B. Lang and A. D. Armour, *Multi-photon resonances in Josephson junction-cavity circuits*, New J. Phys. **23**, 033021 (2021).

[78] L. Arndt and F. Hassler, *Period Tripling due to Parametric Down-Conversion in Circuit QED*, Phys. Rev. Lett. **128**, 187701 (2022).

[79] F. Minganti, V. Savona, and A. Biella, *Dissipative phase transitions in n -photon driven quantum nonlinear resonators*, Quantum **7**, 1170 (2023).

[80] F. Iachello, R. G. Cortiñas, F. Pérez-Bernal, and L. F. Santos, *Symmetries of the squeeze-driven Kerr oscillator*, J. Phys. A: Math. Theor. **56**, 495305 (2023).

[81] L. Guo and V. Peano, *Engineering Arbitrary Hamiltonians in Phase Space*, Phys. Rev. Lett. **132**, 023602 (2024).

[82] A. Labay-Mora, R. Zambrini, and G. L. Giorgi, *Quantum memories for squeezed and coherent superpositions in a driven-dissipative nonlinear oscillator*, Phys. Rev. A **109**, 032407 (2024).

[83] L. Guo, M. Marthaler, and G. Schön, *Phase space crystals: A new way to create a quasienergy band structure*, Phys. Rev. Lett. **111**, 205303 (2013).

[84] L. Guo and P. Liang, *Condensed matter physics in time crystals*, New J. Phys. **22**, 075003 (2020).

[85] K. Sacha, *Time Crystals* (Springer, 2020).

[86] S. Kwon, S. Watabe, and J.-S. Tsai, *Autonomous quantum error correction in a four-photon Kerr parametric oscillator*, npj Quantum Inf. **8**, 40 (2022).

[87] A. Royer, *Wigner function as the expectation value of a parity operator*, Phys. Rev. A **15**, 449–450 (1977).

[88] K. E. Cahill and R. J. Glauber, *Ordered Expansions in Boson Amplitude Operators*, Phys. Rev. **177**, 1857 (1969).

[89] K. E. Cahill and R. J. Glauber, *Density Operators and Quasiprobability Distributions*, Phys. Rev. **177**, 1882 (1969).

[90] A. Miranowicz, J. Kadlec, K. Bartkiewicz, A. Černoch, Y.-N. Chen, K. Lemr, and F. Nori, *Quantifying nonclassicality of vacuum-one-photon superpositions via potentials for Bell nonlocality, quantum steering, and entanglement*, Preprint at <https://doi.org/10.48550/arXiv.2309.12930> (2023).

[91] S. Ahmed, C. Sánchez Muñoz, F. Nori, and A. F. Kockum, *Quantum State Tomography with Conditional Generative Adversarial Networks*, Phys. Rev. Lett. **127**, 140502 (2021).

[92] S. Ahmed, C. Sánchez Muñoz, F. Nori, and A. F. Kockum, *Classification and reconstruction of optical quantum states with deep neural networks*, Phys. Rev. Research **3**, 033278 (2021).

[93] D. P. Kingma and J. Ba, *Adam: A Method for Stochastic Optimization*, Preprint at <https://doi.org/10.48550/arXiv.1412.6980> (2014).

[94] J. R. Johansson, P. D. Nation, and F. Nori, *QuTiP: An open-source Python framework for the dynamics of open quantum systems*, Comp. Phys. Comm. **183**, 1760–1772 (2012).

[95] J. R. Johansson, P. D. Nation, and F. Nori, *QuTiP 2: A Python framework for the dynamics of open quantum systems*, Comp. Phys. Comm. **184**, 1234–1240 (2013).

[96] C. R. Harris, K. Jarrod Millman, S. J. van der Walt, R. Gommers, P. Virtanen, D. Cournapeau, E. Wieser, J. Taylor, S. Berg, N. J. Smith, R. Kern, M. Picus, S. Hoyer, M. H. van Kerkwijk, M. Brett, A. Haldane, J. Fernández del Río, M. Wiebe, P. Peterson, P. Gérard-Marchant, K. Sheppard, T. Reddy, W. Weckesser, H. Abbasi, C. Gohlke, and T. E. Oliphant, *Array programming with NumPy*, Nature **85**, 357–362 (2020).

[97] J. Bradbury, R. Frostig, P. Hawkins, M. J. Johnson, C. Leary, D. Maclaurin, G. Necula, A. Paszke, J. VanderPlas, S. Wanderman-Milne, and Q. Zhang, *JAX: composable transformations of Python+NumPy programs*, <http://github.com/google/jax> (2018).

Acknowledgments: The authors thank Adam Miranowicz, Tsuyoshi Yamamoto, Shiro Saito, Atsushi Noguchi, Shotaro Shirai, and Yoshiki Sunada for their interest in this project and helpful discussion. We also thank Kazumasa Makise of the National Astronomical Observatory of Japan for providing niobium films and the MIT Lincoln Laboratory for providing a Josephson travelling-wave parametric amplifier. This work was primarily supported by the Japan Science and Technology Agency (Moonshot R&D, JPMJMS2067; CREST, JPMJCR1676) and the New Energy and Industrial Technology Development Organization (NEDO, JPNP16007). These funds were secured by JST. SA and AFK acknowledge support from the Knut and Alice Wallenberg Foundation through the Wallenberg Centre for Quantum Technology (WACQT). AFK is also supported by the Swedish Research Council (grant number 2019-03696), the Swedish Foundation for Strategic Research (grant numbers FFL21-0279 and FUS21-0063), and the Horizon Europe programme HORIZON-CL4-2022-QUANTUM-01-SGA via the project 101113946 OpenSuperQPlus100.

Author contributions: SK and JST conceived the project. SK, DH, TN, HM, and JST designed the details of the experiment. DH, TN, and SK performed the measurements and data analysis. TN and SK performed the simulations with contributions from SF. SW provided theoretical support. DH and DI wrote the software for the measurements. SA wrote the code for the density-matrix reconstruction with contributions from AFK and SK. HM managed the hardware. SK and TK designed the chip. TK fabricated the chip. SK wrote the original draft with contributions from DH and TN. All authors contributed to the review and editing of the paper. SK, FY, and JST supervised the project.

Competing interests: The authors declare that they have no competing interests.

Supplementary Information for “Entangling Schrödinger’s cat states by bridging discrete- and continuous-variable encoding”

1. DERIVATION OF THE HAMILTONIAN

In this section, we derive the Hamiltonian of two interacting Kerr parametric oscillators (KPOs). The circuit diagram is shown in Supplementary Fig. 1. The Lagrangian of the circuit is given by

$$\mathcal{L} = \mathcal{T} - \mathcal{U},$$

where

$$\begin{aligned} \mathcal{T} &= \left(\frac{\Phi_0}{2\pi}\right)^2 \left[\frac{C_{s1} + (C_{Ja1} + C_{Jb1})/N_1}{2} \dot{\phi}_1^2 + \frac{C_{s2} + (C_{Ja2} + C_{Jb2})/N_2}{2} \dot{\phi}_2^2 + \frac{C_{int}}{2} (\dot{\phi}_1 - \dot{\phi}_2)^2 \right] \\ &= \frac{C_{K1}}{2} \dot{\phi}_1^2 + \frac{C_{K2}}{2} \dot{\phi}_2^2 - C_{int} \dot{\phi}_1 \dot{\phi}_2, \\ \mathcal{U} &= -N_1 E_{Ja1} \cos\left(\frac{\phi_1}{N_1} - r_{a1} \varphi_{ex1}\right) - N_1 E_{Jb1} \cos\left(\frac{\phi_1}{N_1} + r_{b1} \varphi_{ex1}\right) \\ &\quad - N_2 E_{Ja2} \cos\left(\frac{\phi_2}{N_2} - r_{a2} \varphi_{ex2}\right) - N_2 E_{Jb2} \cos\left(\frac{\phi_2}{N_2} + r_{b2} \varphi_{ex2}\right). \end{aligned}$$

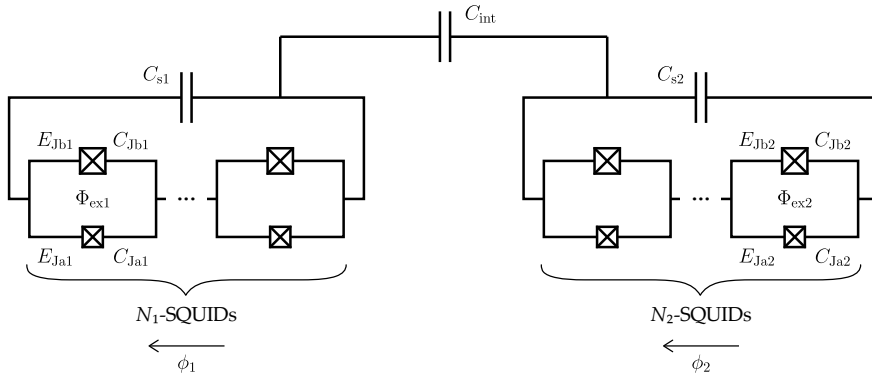
Here, Φ_0 is the magnetic flux quantum, $C_{Ki} \equiv (\Phi_0/2\pi)^2 [C_{si} + (C_{Ja_i} + C_{Jb_i})/N_i + C_{int}]$, $C_{int} \equiv (\Phi_0/2\pi)^2 C_{int}$, $\varphi_{exi} \equiv 2\pi\Phi_{exi}/\Phi_0$, and $r_{ai} + r_{bi} = 1$ ($i = 1, 2$), where these scaling parameters are determined by the irrotational constraint [1]. Note that all capacitances are renormalized by a factor of $(\Phi_0/2\pi)^2$. Using the formula $A \cos(x) + B \sin(x) = R \cos(x - \lambda)$, where $R = \sqrt{A^2 + B^2}$ and $\tan(\lambda) = B/A$, we obtain

$$\mathcal{U} = -N_1 E_{J1} \cos\left(\frac{\phi_1}{N_1} - \lambda_1\right) - N_2 E_{J2} \cos\left(\frac{\phi_2}{N_2} - \lambda_2\right),$$

where

$$\begin{aligned} E_{Ji} &= \sqrt{E_{Ja_i}^2 + E_{Jb_i}^2 + 2E_{Ja_i}E_{Jb_i} \cos(\varphi_{exi})}, \\ \lambda_i &= \arctan\left(\frac{E_{Ja_i} \sin(r_{ai} \varphi_{exi}) - E_{Jb_i} \sin(r_{bi} \varphi_{exi})}{E_{Ja_i} \cos(r_{ai} \varphi_{exi}) + E_{Jb_i} \cos(r_{bi} \varphi_{exi})}\right). \end{aligned}$$

To account for the flux-bias modulation, we decompose φ_{exi} into static and oscillating parts, i.e., $\varphi_{dc_i} + \varphi_{aci}(t)$. The oscillating part is the parametric pump given by $\varphi_{aci}(t) = 2\varphi_{aci}^{(0)} \cos(\omega_{pi}t + \theta_{pi})$, where ω_{pi} and θ_{pi} are



Supplementary Fig. 1: Circuit diagram of a superconducting KPO. The KPO consists of N_i direct-current superconducting quantum interference devices (DC SQUIDs), where $i = 1, 2$. E_{Ja_i} and C_{Ja_i} (E_{Jb_i} and C_{Jb_i}) represent the Josephson energy and the capacitance of the smaller (larger) junction in each DC SQUID, respectively. C_{si} denotes the shunting capacitance of the KPO, C_{int} is the coupling capacitance between the two KPOs, and Φ_{exi} is the external magnetic flux threaded through one DC SQUID.

the frequency and phase of the pump applied to KPO*i*, respectively. Then, we introduce a variable change, $\phi_{\text{dci}} \rightarrow \phi_{\text{dci}} + N_i \lambda_i$. The oscillating part of λ_i is ignored here because the terms associated with it disappear after the rotating-wave approximation [2]. Since $\varphi_{\text{aci}}^{(0)} \ll 2\pi$, we take the Taylor expansion at $\varphi_{\text{exi}} = \varphi_{\text{dci}}$:

$$\mathcal{U} \approx -N_1 \left(E_{\text{J}1}^{(0)} + E_{\text{J}1}^{(1)} \varphi_{\text{aci}} + E_{\text{J}1}^{(2)} \varphi_{\text{aci}}^2 \right) \cos\left(\frac{\phi_1}{N_1}\right) - N_2 \left(E_{\text{J}2}^{(0)} + E_{\text{J}2}^{(1)} \varphi_{\text{aci}} + E_{\text{J}2}^{(2)} \varphi_{\text{aci}}^2 \right) \cos\left(\frac{\phi_2}{N_2}\right),$$

where

$$\begin{aligned} E_{\text{J}i}^{(0)} &= \sqrt{E_{\text{J}ai}^2 + E_{\text{J}bi}^2 + 2E_{\text{J}ai}E_{\text{J}bi} \cos(\varphi_{\text{dci}})}, \\ E_{\text{J}i}^{(1)} &= -\frac{1}{E_{\text{J}i}^{(0)}} E_{\text{J}ai}E_{\text{J}bi} \sin(\varphi_{\text{dci}}), \\ E_{\text{J}i}^{(2)} &= -\frac{1}{2(E_{\text{J}i}^{(0)})^3} [E_{\text{J}ai}E_{\text{J}bi}(E_{\text{J}ai}^2 + E_{\text{J}bi}^2) \cos(\varphi_{\text{dci}}) + (E_{\text{J}ai}E_{\text{J}bi})^2 \{\cos^2(\varphi_{\text{dci}}) + 1\}]. \end{aligned}$$

Here, the φ_{aci} terms give the parametric pump, whereas the φ_{aci}^2 terms induce a small frequency shift, which we refer to as an AC Stark-like frequency shift for convenience.

The conjugate number operators are defined by

$$\hbar N_{\phi 1} = \frac{\partial \mathcal{L}}{\partial \dot{\phi}_1} = C_{\text{K}1} \dot{\phi}_1 - C_{\text{int}} \dot{\phi}_2, \quad \hbar N_{\phi 2} = \frac{\partial \mathcal{L}}{\partial \dot{\phi}_2} = -C_{\text{int}} \dot{\phi}_1 + C_{\text{K}2} \dot{\phi}_2,$$

where the reduced Planck constants are inserted to make $N_{\phi 1}$ and $N_{\phi 2}$ dimensionless. In matrix form,

$$\hbar \begin{pmatrix} N_{\phi 1} \\ N_{\phi 2} \end{pmatrix} = \begin{pmatrix} C_{\text{K}1} & -C_{\text{int}} \\ -C_{\text{int}} & C_{\text{K}2} \end{pmatrix} \begin{pmatrix} \dot{\phi}_1 \\ \dot{\phi}_2 \end{pmatrix}.$$

Using the inverse capacitance matrix, we obtain

$$\begin{pmatrix} \dot{\phi}_1 \\ \dot{\phi}_2 \end{pmatrix} = \frac{\hbar}{C_{\text{K}1}C_{\text{K}2} - C_{\text{int}}^2} \begin{pmatrix} C_{\text{K}2} & C_{\text{int}} \\ C_{\text{int}} & C_{\text{K}1} \end{pmatrix} \begin{pmatrix} N_{\phi 1} \\ N_{\phi 2} \end{pmatrix}.$$

The resulting Hamiltonian is (hereafter, we add a hat to an operator for clarity)

$$\begin{aligned} \hat{\mathcal{H}} = & 4E_{\text{C}1}\hat{N}_{\phi 1}^2 + 4E_{\text{C}2}\hat{N}_{\phi 2}^2 + 8E_{\text{int}}\hat{N}_{\phi 1}\hat{N}_{\phi 2} \\ & - N_1 E_{\text{K}1} \cos\left(\frac{\hat{\phi}_1}{N_1}\right) - 2\gamma_1 \cos(\omega_{\text{p}1}t + \theta_{\text{p}1}) \cos\left(\frac{\hat{\phi}_1}{N_1}\right) - N_2 E_{\text{K}2} \cos\left(\frac{\hat{\phi}_2}{N_2}\right) - 2\gamma_2 \cos(\omega_{\text{p}2}t + \theta_{\text{p}2}) \cos\left(\frac{\hat{\phi}_2}{N_2}\right), \end{aligned}$$

where

$$E_{\text{C}1} \equiv \frac{\hbar^2 C_{\text{K}2}}{8(C_{\text{K}1}C_{\text{K}2} - C_{\text{int}}^2)}, \quad E_{\text{C}2} \equiv \frac{\hbar^2 C_{\text{K}1}}{8(C_{\text{K}1}C_{\text{K}2} - C_{\text{int}}^2)}, \quad E_{\text{int}} \equiv \frac{\hbar^2 C_{\text{int}}}{8(C_{\text{K}1}C_{\text{K}2} - C_{\text{int}}^2)}.$$

Here, we define $E_{\text{K}i} \equiv E_{\text{J}i}^{(0)} + 2E_{\text{J}i}^{(2)}(\varphi_{\text{aci}}^{(0)})^2$ and $\gamma_i \equiv N_i E_{\text{J}i}^{(1)} \varphi_{\text{aci}}^{(0)}$. The φ_{aci}^2 term is averaged out by using $\langle \varphi_{\text{aci}}^2 \rangle = 2(\varphi_{\text{aci}}^{(0)})^2$ and absorbed into $E_{\text{K}i}$.

We move to the occupation-number representation by defining

$$\hat{N}_{\phi i} = iN_{\phi i}^{(0)}(\hat{a}_i^\dagger - \hat{a}_i) \quad \text{and} \quad \hat{\phi}_i = \phi_i^{(0)}(\hat{a}_i^\dagger + \hat{a}_i),$$

where $N_{\phi i}^{(0)} = \sqrt[4]{E_{\text{K}i}/32N_iE_{\text{C}i}}$ and $\phi_i^{(0)} = \sqrt[4]{2N_iE_{\text{C}i}/E_{\text{K}i}}$ are the zero-point fluctuations. Then we have

$$\begin{aligned} \hat{\mathcal{H}} = & \hbar\omega_{\text{K}1}^{(0)}\hat{a}_1^\dagger\hat{a}_1 + \hbar\omega_{\text{K}2}^{(0)}\hat{a}_2^\dagger\hat{a}_2 + \hbar g(\hat{a}_1^\dagger\hat{a}_2 + \hat{a}_1\hat{a}_2^\dagger - \hat{a}_1\hat{a}_2 - \hat{a}_1^\dagger\hat{a}_2^\dagger) \\ & - N_1 E_{\text{K}1} \left[1 + \frac{1}{24} \left(\frac{\hat{\phi}_1}{N_1} \right)^4 - \dots \right] - 2\gamma_1 \cos(\omega_{\text{p}1}t + \theta_{\text{p}1}) \left[1 - \frac{1}{2} \left(\frac{\hat{\phi}_1}{N_1} \right)^2 + \frac{1}{24} \left(\frac{\hat{\phi}_1}{N_1} \right)^4 - \dots \right] \\ & - N_2 E_{\text{K}2} \left[1 + \frac{1}{24} \left(\frac{\hat{\phi}_2}{N_2} \right)^4 - \dots \right] - 2\gamma_2 \cos(\omega_{\text{p}2}t + \theta_{\text{p}2}) \left[1 - \frac{1}{2} \left(\frac{\hat{\phi}_2}{N_2} \right)^2 + \frac{1}{24} \left(\frac{\hat{\phi}_2}{N_2} \right)^4 - \dots \right], \end{aligned}$$

where

$$\hbar\omega_{\text{Ki}}^{(0)} \equiv \sqrt{\frac{8E_{\text{Ci}}E_{\text{Ki}}}{N_i}}, \quad \hbar g \equiv E_{\text{int}} \sqrt[4]{\frac{4E_{\text{K1}}E_{\text{K2}}}{N_1N_2E_{\text{C1}}E_{\text{C2}}}} = \frac{1}{2} \frac{E_{\text{int}}}{\sqrt{E_{\text{C1}}E_{\text{C2}}}} \sqrt{\omega_{\text{K1}}^{(0)}\omega_{\text{K2}}^{(0)}}. \quad (1)$$

By using the formula (derived on the basis of Ref. [3])

$$(\hat{a}^\dagger \pm \hat{a})^n = \sum_{k=0}^n \sum_{m=0}^{\lfloor \frac{k}{2} \rfloor} \frac{(\pm 1)^{m-k} n!}{(n-k)!(k-2m)!m!2^m} (\hat{a}^\dagger)^{k-2m} \hat{a}^{n-k},$$

we obtain

$$\begin{aligned} -\frac{E_{\text{Ki}}}{24N_i^3} \hat{\phi}_i^4 &\Rightarrow -\hbar K_i \hat{a}_i^\dagger \hat{a}_i - \frac{\hbar K_i}{2} \hat{a}_i^\dagger \hat{a}_i^\dagger \hat{a}_i \hat{a}_i \\ &\quad - \frac{\hbar K_i}{12} \left(6\hat{a}_i^\dagger \hat{a}_i^\dagger + 6\hat{a}_i \hat{a}_i + 4\hat{a}_i^\dagger \hat{a}_i \hat{a}_i \hat{a}_i + 4\hat{a}_i^\dagger \hat{a}_i^\dagger \hat{a}_i \hat{a}_i + \hat{a}_i \hat{a}_i \hat{a}_i \hat{a}_i + \hat{a}_i^\dagger \hat{a}_i^\dagger \hat{a}_i^\dagger \hat{a}_i^\dagger \right), \\ \frac{\gamma_i}{N_i^2} \cos(\omega_{\text{pi}} t + \theta_{\text{pi}}) \hat{\phi}_i^2 &\Rightarrow \hbar P_i \cos(\omega_{\text{pi}} t + \theta_{\text{pi}}) \left(2\hat{a}_i^\dagger \hat{a}_i + \hat{a}_i^\dagger \hat{a}_i^\dagger + \hat{a}_i \hat{a}_i \right), \end{aligned} \quad (2)$$

where $\hbar K_i \equiv E_{\text{Ci}}/N_i^2$ and $\hbar P_i \equiv \varphi_{\text{aci}}^{(0)} E_{\text{Ji}}^{(1)} \sqrt{2E_{\text{Ci}}/N_i E_{\text{Ki}}}$.

Now we move to the rotating frame whose Hamiltonian is defined by

$$\hat{\mathcal{H}}_0/\hbar = \frac{\omega_{\text{p1}}}{2} \hat{a}_1^\dagger \hat{a}_1 + \frac{\omega_{\text{p2}}}{2} \hat{a}_2^\dagger \hat{a}_2$$

and make the rotating-wave approximation. Then, the surviving terms are

$$\begin{aligned} \hat{\mathcal{H}}_{\text{rot}}/\hbar &= e^{i\hat{\mathcal{H}}_0 t/\hbar} (\hat{\mathcal{H}} - \hat{\mathcal{H}}_0) e^{-i\hat{\mathcal{H}}_0 t/\hbar} \times (1/\hbar) \\ &\approx \Delta_1 \hat{a}_1^\dagger \hat{a}_1 - \frac{K_1}{2} \hat{a}_1^\dagger \hat{a}_1^\dagger \hat{a}_1 \hat{a}_1 + \frac{P_1}{2} \left(\hat{a}_1^\dagger \hat{a}_1^\dagger + \hat{a}_1 \hat{a}_1 \right) + \Delta_2 \hat{a}_2^\dagger \hat{a}_2 - \frac{K_2}{2} \hat{a}_2^\dagger \hat{a}_2^\dagger \hat{a}_2 \hat{a}_2 + \frac{P_2}{2} \left(\hat{a}_2^\dagger \hat{a}_2^\dagger + \hat{a}_2 \hat{a}_2 \right) \\ &\quad + g \left[\hat{a}_1^\dagger \hat{a}_2 e^{+i(\Delta_{\text{p}} t + \theta_{\text{p}})} + \hat{a}_1 \hat{a}_2^\dagger e^{-i(\Delta_{\text{p}} t + \theta_{\text{p}})} \right]. \end{aligned} \quad (3)$$

Here, $\Delta_i (\equiv \omega_{\text{Ki}} - \omega_{\text{pi}}/2)$ is the KPO-pump frequency detuning, where $\omega_{\text{Ki}} (\equiv \omega_{\text{Ki}}^{(0)} - K_i)$ is the transition frequency between the $|0_F\rangle$ and $|1_F\rangle$ states; $\Delta_{\text{p}} \equiv (\omega_{\text{p1}} - \omega_{\text{p2}})/2$ and $\theta_{\text{p}} \equiv (\theta_{\text{p1}} - \theta_{\text{p2}})/2$. Note that the unitary transformation $\hat{a}_i \rightarrow \hat{a}_i e^{-i\theta_{\text{pi}}/2}$ was performed. Setting $\theta_{\text{p}} = 0$ gives Eq. (1) in the main text.

2. SYSTEM PARAMETERS

The measured system parameters are presented in Supplementary Table 1. The Hamiltonian was characterized by analysing Rabi oscillations in the $|0_F\rangle$ state population, following the methodology outlined in Ref. [6], except for the coupling constant g . The value of g was determined by tuning the global flux bias to the point where the transition frequency of both KPOs becomes equal and then observing the anti-crossing in the KPO signal. At this flux bias, where $\omega_{\text{K1}}/2\pi = \omega_{\text{K2}}/2\pi = 2.237$ GHz, $g/2\pi$ was found to be 7.2 MHz. Consequently, the coupling constant at our working flux bias, where $\omega_{\text{K1}}/2\pi = 2.564$ GHz and $\omega_{\text{K2}}/2\pi = 2.420$ GHz, would be 8.0 MHz, according to Supplementary Eq. (1).

The calibration between the AWG setting value and the displacement in phase space was achieved by fitting the parity measurement of the vacuum state with the following Hamiltonian [5, 6]:

$$\begin{aligned} \hat{\mathcal{H}}_{\text{fit}i}/\hbar &= \Delta_{\text{Ki}} \hat{a}_i^\dagger \hat{a}_i - \frac{K_i}{2} \hat{a}_i^\dagger \hat{a}_i^\dagger \hat{a}_i \hat{a}_i + \beta_i \left(\hat{a}_i^\dagger e^{-i\Delta_{\text{dT}i} t} + \hat{a}_i e^{+i\Delta_{\text{dT}i} t} \right) \\ &\quad + \hbar \Delta_{\text{T}i} \hat{b}_i^\dagger \hat{b}_i - \frac{K_{\text{T}i}}{2} \hat{b}_i^\dagger \hat{b}_i^\dagger \hat{b}_i \hat{b}_i + \beta_{\text{T}i} (\hat{b}_i^\dagger + \hat{b}_i) + \chi_{\text{KT}i} \hat{a}_i^\dagger \hat{a}_i \hat{b}_i^\dagger \hat{b}_i + \chi_{\text{KKT}i} \hat{a}_i^\dagger \hat{a}_i (\hat{a}_i^\dagger \hat{a}_i - 1) \hat{b}_i^\dagger \hat{b}_i. \end{aligned} \quad (4)$$

Here, $\Delta_{\text{Ki}} \equiv \omega_{\text{Ki}} - \omega_{\text{Tdi}}$, where ω_{Tdi} is the frequency of the drive for transmoni ($i = 1, 2$); $\Delta_{\text{dT}i} \equiv \omega_{\text{di}} - \omega_{\text{Tdi}}$; and $\Delta_{\text{T}i} \equiv \omega_{\text{T}i} - \omega_{\text{Tdi}}$. For more details, see Ref. [6].

Supplementary Table 1: Measured system parameters. Φ_0 is the magnetic flux quantum. “RR” stands for readout resonator. For the self-Kerr coefficient of the KPOs, the value in parentheses is the coefficient when the pump is on. For more rigorous definitions, see Supplementary Eqs. (3) and (4).

Physical quantity	Symbol	System 1	System 2
Number of DC SQUIDS in KPO	N_i	10	10
External magnetic flux threaded through one DC SQUID	Φ_{exi}	$0.229\Phi_0$	$0.191\Phi_0$
Transition frequency between the $ 0\rangle$ and $ 1\rangle$ states of KPO	$\omega_{\text{K}i}/2\pi$	2.5635 GHz	2.4199 GHz
Self-Kerr coefficient of KPO	$K_i/2\pi$	2.86 (2.05) MHz	2.91 (1.90) MHz
Longitudinal relaxation time of KPO	$T_1^{\text{K}i}$	$13 \pm 3 \mu\text{s}$	$20 \pm 6 \mu\text{s}$
Transverse relaxation time of KPO	$T_2^{\text{K}i}$	$4.8 \pm 0.4 \mu\text{s}$	$4.3 \pm 0.8 \mu\text{s}$
Coupling constant between two KPOs	$g/2\pi$	8.0 MHz	
Transition frequency between $ g\rangle$ and $ e\rangle$ states of transmon	$\omega_{\text{T}i}/2\pi$	3.8076 GHz	3.6216 GHz
Anharmonicity of transmon	$K_{\text{T}i}/2\pi$	221.3 MHz	225.9 MHz
Longitudinal relaxation time of transmon	$T_1^{\text{T}i}$	$49 \pm 7 \mu\text{s}$	$37 \pm 4 \mu\text{s}$
Transverse relaxation time of transmon	$T_2^{\text{T}i}$	$25 \pm 2 \mu\text{s}$	$13 \pm 1 \mu\text{s}$
Cross-Kerr coefficient between KPO and transmon	$\chi_{\text{KKT}i}/2\pi$	1.69 MHz	1.72 MHz
Higher-order cross-Kerr coefficient	$\chi_{\text{KKT}i}/2\pi$	-7 kHz	-7 kHz
Number of thermally excited photons in KPO	n_{thi}	0.09	0.08
Resonance frequency of RR	$\omega_{\text{R}i}/2\pi$	7.6079 GHz	7.4641 GHz
Cross-Kerr coefficient between transmon and RR	$\chi_{\text{TR}i}/2\pi$	0.37 MHz	0.39 MHz

3. FULL PULSE SEQUENCE

The full pulse sequence, including that for Wigner-function measurement via the Lutterbach–Davidovich method [7–9], is depicted in Supplementary Fig. 2. Specific details regarding pulse shapes are outlined in Supplementary Table 2. Notably, a 340 ns delay is introduced between the displacement pulse for KPO1 and the first $\pi/2$ pulse for transmon1 to prevent the unintended excitation of transmon1 triggered by the $\pi/2$ pulses for transmon2. This precaution is necessary owing to the small frequency difference (only 35 MHz) between the $|e\rangle$ - $|f\rangle$ transition of transmon1 and the $|g\rangle$ - $|e\rangle$ transition of transmon2, falling within the bandwidth of the $\pi/2$ pulses for Wigner function measurement. By comparing two one-mode Wigner function measurements of KPO1—one obtained from the simultaneous measurement of both transmons with the delay, and the other from the transmon1 measurement only without the delay—we found that this delay does not severely degrade the quality of the Wigner function measurement, as the Kerr evolution preserves the number parity.

4. SIMULATION OF BELL–CAT STATE GENERATION

A. Conversion from Fock to cat

We simulate our Bell–Cat generation scheme via conversion from Fock states to cat states by solving the following Lindblad master equation with QuTiP [10, 11]:

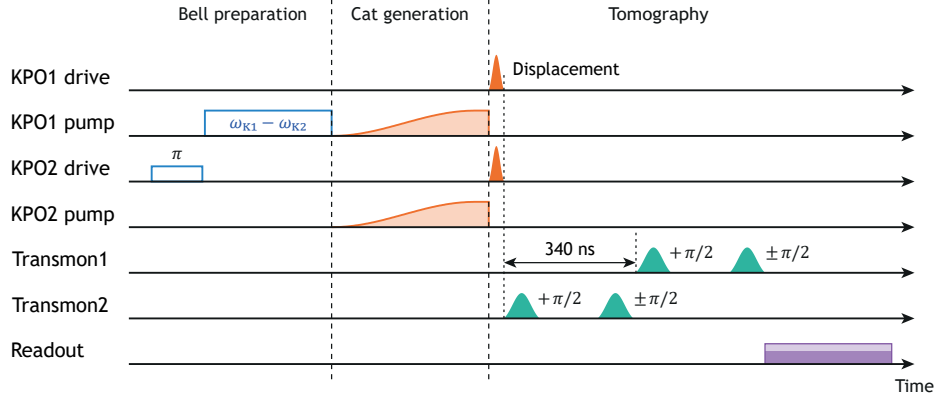
$$\frac{\partial \rho(t)}{\partial t} = -\frac{i}{\hbar} [\hat{\mathcal{H}}(t), \rho(t)] + \{\gamma_{\text{K}1}\mathcal{D}[\hat{a}_1] + \gamma_{\text{K}2}\mathcal{D}[\hat{a}_2] + \gamma_{\phi 1}\mathcal{D}[\hat{a}_1^\dagger \hat{a}_1] + \gamma_{\phi 2}\mathcal{D}[\hat{a}_2^\dagger \hat{a}_2]\}\rho(t), \quad (5)$$

where ρ is the density matrix of the two-KPO system, $\mathcal{D}[\hat{O}]\rho = \hat{O}\rho\hat{O}^\dagger - \frac{1}{2}\hat{O}^\dagger\hat{O}\rho - \frac{1}{2}\rho\hat{O}^\dagger\hat{O}$, $\gamma_{\text{K}i}$ is the single-photon loss rate of KPO*i*, and $\gamma_{\phi i}$ is the dephasing rate of KPO*i* ($i = 1, 2$).

We first simulate the Bell–Fock state preparation. In a frame rotating with the frequency $\omega_{\text{K}1}$, the Hamiltonian describing the Bell-preparation pulse for the $|0_{\text{F}}1_{\text{F}}\rangle \pm |1_{\text{F}}0_{\text{F}}\rangle$ state is given by

$$\begin{aligned} \hat{\mathcal{H}}_{\text{BFD}}/\hbar = & -\frac{K_1}{2}\hat{a}_1^\dagger \hat{a}_1^\dagger \hat{a}_1 \hat{a}_1 + (\omega_{\text{K}2} - \omega_{\text{K}1})\hat{a}_2^\dagger \hat{a}_2 - \frac{K_2}{2}\hat{a}_2^\dagger \hat{a}_2^\dagger \hat{a}_2 \hat{a}_2 \\ & + g(\hat{a}_1^\dagger \hat{a}_2 + \hat{a}_1 \hat{a}_2^\dagger) + 2P_g \cos[(\omega_{\text{K}1} - \omega_{\text{K}2} + \delta_g)t + \theta_g] \hat{a}_1^\dagger \hat{a}_1. \end{aligned} \quad (6)$$

Here, P_g and θ_g represent the amplitude and phase of the pulse, respectively. The factor of 2 preceding P_g originates from Supplementary Eq. (2). A small detuning, $\delta_g/2\pi = 0.88$ MHz, was used in the simulation to align the pulse frequency with the centre frequency of the Rabi pattern.



Supplementary Fig. 2: Full pulse sequence of Fig. 2c. In the “tomography” part, the displacement pulses applied to both KPOs implement the displacement operators described in Eqs. (2) and (3) in the main text. The subsequent $\pi/2$ pulses applied to the transmons map the number parity of the KPOs to the transmon states. Then, the states of the two transmons are measured simultaneously. For this measurement, two microwave pulses with the frequencies of the readout resonators are combined and applied to the chip. Regarding the 340 ns delay in the transmon1 pulse sequence, see the supplementary text.

Supplementary Table 2: Parameters for the pulse shape. “ σ ” represents the standard deviation of Gaussian pulses. For flap-top Gaussian pulses, σ indicates the standard deviation of the pulse edges. The time intervals between two $\pi/2$ transmon pulses for the parity measurement are 278 ns for KPO1 and 280 ns for KPO2.

Operation	Data	Element	Pulse shape	Pulse length (ns)	σ (ns)
Cat generation	Figs. 1–3	KPO	$\sin^2(\pi t/2\tau_{\text{ramp}})$	1000	
Bell preparation	Fig. 2 ($ 0_F 1_F\rangle$)	KPO2	Flat-top Gaussian	955	1
	Fig. 2 ($ 0_F 1_F\rangle \pm 1_F 0_F\rangle$)	KPO1	Flat-top Gaussian	730	1
	Fig. 2 ($ 0_F 0_F\rangle \pm 1_F 1_F\rangle$)	KPO1	Flat-top Gaussian	852	1
Two-cat Rabi $\sqrt{i\text{SWAP}}$ gate	Fig. 3	KPO1	Flat-top Gaussian	Variable	1
				275	1
Parity measurement	All Wigner functions	KPO	Gaussian	10	2.5
		Transmon	Gaussian ($\pi/2$)	25	6.25
Rabi	Fig. 4	KPO	Flat-top Gaussian	Variable	1
		Transmon	Gaussian (π)	2000	500
Transmon readout	All data	Readout resonator	Flat-top Gaussian	2500	4

The $|0_F 0_F\rangle \pm |1_F 1_F\rangle$ state preparation can also be simulated similarly by using the following Hamiltonian in a frame rotating with the frequency $(\omega_{K1} + \omega_{K2})/2$:

$$\hat{\mathcal{H}}_{\text{BFS}}/\hbar = \left(\frac{\omega_{K1} - \omega_{K2}}{2} + \delta_g \right) \hat{a}_1^\dagger \hat{a}_1 - \frac{K_1}{2} \hat{a}_1^\dagger \hat{a}_1^\dagger \hat{a}_1 \hat{a}_1 + \left(\frac{\omega_{K2} - \omega_{K1}}{2} + \delta_g \right) \hat{a}_2^\dagger \hat{a}_2 - \frac{K_2}{2} \hat{a}_2^\dagger \hat{a}_2^\dagger \hat{a}_2 \hat{a}_2 + g \left(\hat{a}_1^\dagger \hat{a}_2 + \hat{a}_1 \hat{a}_2^\dagger \right) + \frac{P_g}{2} \left(\hat{a}_1^\dagger \hat{a}_1^\dagger e^{-i\theta_g} + \hat{a}_1 \hat{a}_1 e^{+i\theta_g} \right), \quad (7)$$

where $\delta_g/2\pi = -30$ kHz in our simulation.

Next, we simulate the cat generation process by solving Supplementary Eq. (5) with Supplementary Eq. (3), using the result of the Bell-Fock preparation simulation with Eq. (6) or (7) as the initial state. The coupling term in Supplementary Eq. (3) was omitted at this step because, without a Bell-preparation or gate pulse, its contribution would be averaged out.

Supplementary Table 3 summarises the infidelity between the measured and target states due to thermal excitation, single-photon loss, and dephasing estimated through these simulations. Two-mode Wigner functions for the target states and selected simulated states are presented in Supplementary Figs. 3 and 4, respectively.

Supplementary Table 3: Impact of error sources on the fidelity between the measured and target states. The values represent infidelities estimated through simulations that selectively included or excluded the Lindblad operators in Eq. (5). The column labelled “Thermal excitation” indicates the infidelity between the vacuum state and the tensor-product thermal states of both KPOs, while “Imperfect operation” reflects infidelity due to imperfect control arising from the small Kerr coefficient. For cat generation process, dephasing is not considered because low-frequency noise does not affect the fidelity as pointed out in the main text. Values from Supplementary Tables 1 and 2 were used for the simulation. In our simulations, these infidelities were found to be additive. Consequently, the resulting fidelity of the simulated Bell–Cat states ranges from 0.66 to 0.70, depending on the presence of the π -pulse. Em dashes denote “not applicable.”

Step	Thermal excitation	Single-photon loss	Dephasing	Imperfect operation
Vacuum state preparation	0.14	—	—	—
π -pulse on KPO2	—	0.01	0.02	0.01
Bell preparation	—	0.01	0.02	0.01
Cat generation	—	0.08	—	0.03

B. Two-cat gate operation

To simulate two-cat Rabi oscillations, it is convenient to express the Hamiltonian for our two-cat gate operation in the following form [4]:

$$\hat{\mathcal{H}}_g/\hbar = 2P_g \cos(\omega_g t + \theta_g) \hat{a}_1^\dagger \hat{a}_1 = 2P_g \cos[(\Delta_p + \Delta_g)t + \theta_g] \hat{a}_1^\dagger \hat{a}_1, \quad (8)$$

where $\Delta_g \equiv \omega_g - \Delta_p$. The results in Fig. 5a were obtained using Supplementary Eqs. (3), (8), and (5).

5. TWO-CAT RABI OSCILLATIONS IN INTERACTING TWO-LEVEL SYSTEM QUBITS

As mentioned in the main text, the two-cat Rabi oscillations can be reproduced in interacting two-level qubits, whose resonance frequencies are ω_{q1} and ω_{q2} . We first consider $|0_F 1_F\rangle \leftrightarrow |1_F 0_F\rangle$ transitions induced by the parametric modulation of the coupling constant with the frequency ω_g . The Hamiltonian describing this process is given by [12]

$$\hat{\mathcal{H}}_{Rs}/\hbar = J_g \cos[(\Delta_q + \Delta_g)t] (\hat{\sigma}_+^{(1)} \hat{\sigma}_-^{(2)} e^{+i\Delta_q t} + \hat{\sigma}_-^{(1)} \hat{\sigma}_+^{(2)} e^{-i\Delta_q t}), \quad (9)$$

where J_g is the modulation amplitude of the coupling constant, $\Delta_q \equiv \omega_{q1} - \omega_{q2}$, $\Delta_g \equiv \omega_g - \Delta_q$, and $\hat{\sigma}_\pm^{(k)} \equiv (\hat{\sigma}_x^{(k)} \pm i\hat{\sigma}_y^{(k)})/2$, where $\hat{\sigma}_x^{(k)}$ and $\hat{\sigma}_y^{(k)}$ are the Pauli operators of qubit k ($k = 1, 2$). To reproduce our data for $|0_C 1_C\rangle \leftrightarrow |1_C 0_C\rangle$ transitions, we need two modulation tones with opposite detuning:

$$\hat{\mathcal{H}}_{Rd}/\hbar = \frac{J_g}{2} [\cos\{(\Delta_q + \Delta_g)t\} + \cos\{(\Delta_q - \Delta_g)t\}] (\hat{\sigma}_+^{(1)} \hat{\sigma}_-^{(2)} e^{+i\Delta_q t} + \hat{\sigma}_-^{(1)} \hat{\sigma}_+^{(2)} e^{-i\Delta_q t}). \quad (10)$$

Here, the frequency $\Delta_q + \Delta_g$ corresponds to ω_g and the frequency $\Delta_q - \Delta_g$ corresponds to $2(\omega_{q1} - \omega_{q2}) - \omega_g$. The simulations using Supplementary Eqs. (9) and (10) are shown in Supplementary Fig. 5b.

6. TWO-CAT GATE OPERATION IN MATRIX FORM

Here, we present the mathematical form of our two-cat gate operation. The gate, originally proposed in Ref. [4], corresponds to an $\hat{R}_{ZZ}(2\Theta)$ operation in the coherent-state basis $|\pm\alpha\rangle$, which we denote as $|0_\alpha\rangle$ and $|1_\alpha\rangle$, respectively:

$$\hat{R}_{ZZ}(2\Theta) = \begin{vmatrix} |0_\alpha 0_\alpha\rangle & \langle 0_\alpha 0_\alpha| & \langle 0_\alpha 1_\alpha| & \langle 1_\alpha 0_\alpha| & \langle 1_\alpha 1_\alpha| \\ |0_\alpha 1_\alpha\rangle & e^{-i\Theta} & & & \\ |1_\alpha 0_\alpha\rangle & & e^{i\Theta} & & \\ |1_\alpha 1_\alpha\rangle & & & e^{i\Theta} & \\ & & & & e^{-i\Theta} \end{vmatrix}.$$

In the coherent state basis, the cat-state basis is expressed as follows:

$$\begin{aligned} |0_C0_C\rangle &= \frac{1}{2}(|0_\alpha0_\alpha\rangle + |0_\alpha1_\alpha\rangle + |1_\alpha0_\alpha\rangle + |1_\alpha1_\alpha\rangle) \\ |0_C1_C\rangle &= \frac{1}{2}(|0_\alpha0_\alpha\rangle - |0_\alpha1_\alpha\rangle + |1_\alpha0_\alpha\rangle - |1_\alpha1_\alpha\rangle) \\ |1_C0_C\rangle &= \frac{1}{2}(|0_\alpha0_\alpha\rangle + |0_\alpha1_\alpha\rangle - |1_\alpha0_\alpha\rangle - |1_\alpha1_\alpha\rangle) \\ |1_C1_C\rangle &= \frac{1}{2}(|0_\alpha0_\alpha\rangle - |0_\alpha1_\alpha\rangle - |1_\alpha0_\alpha\rangle + |1_\alpha1_\alpha\rangle) \end{aligned}$$

Thus, the transformation between the coherent- and cat-state basis for an arbitrary wavefunction $|\psi\rangle$ is given by

$$\begin{pmatrix} \langle 0_C0_C|\psi\rangle \\ \langle 0_C1_C|\psi\rangle \\ \langle 1_C0_C|\psi\rangle \\ \langle 1_C1_C|\psi\rangle \end{pmatrix} = \underbrace{\frac{1}{2} \begin{pmatrix} 1 & 1 & 1 & 1 \\ 1 & -1 & 1 & -1 \\ 1 & 1 & -1 & -1 \\ 1 & -1 & -1 & 1 \end{pmatrix}}_{\hat{U}_T} \begin{pmatrix} \langle 0_\alpha0_\alpha|\psi\rangle \\ \langle 0_\alpha1_\alpha|\psi\rangle \\ \langle 1_\alpha0_\alpha|\psi\rangle \\ \langle 1_\alpha1_\alpha|\psi\rangle \end{pmatrix},$$

where \hat{U}_T is the transformation matrix.

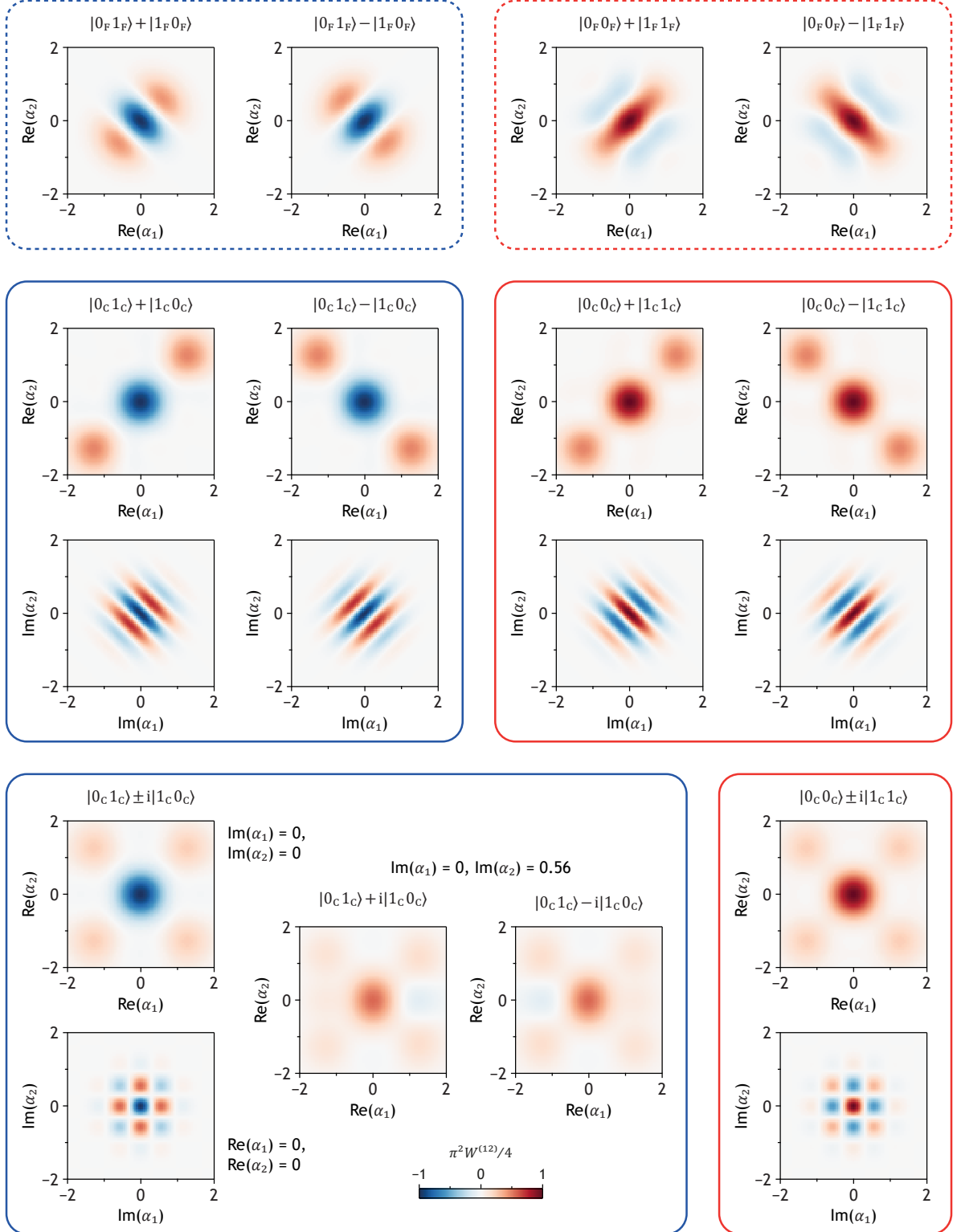
The \hat{R}_{ZZ} gate in the cat-state basis is expressed as

$$\hat{U}_G = \hat{U}_T^\dagger \hat{R}_{ZZ}(2\Theta) \hat{U}_T = \begin{pmatrix} |0_C0_C\rangle \\ |0_C1_C\rangle \\ |1_C0_C\rangle \\ |1_C1_C\rangle \end{pmatrix} \begin{pmatrix} \langle 0_C0_C| & \langle 0_C1_C| & \langle 1_C0_C| & \langle 1_C1_C| \\ \cos(\Theta) & & & -i\sin(\Theta) \\ & \cos(\Theta) & -i\sin(\Theta) & \\ -i\sin(\Theta) & & \cos(\Theta) & \\ -i\sin(\Theta) & & & \cos(\Theta) \end{pmatrix}.$$

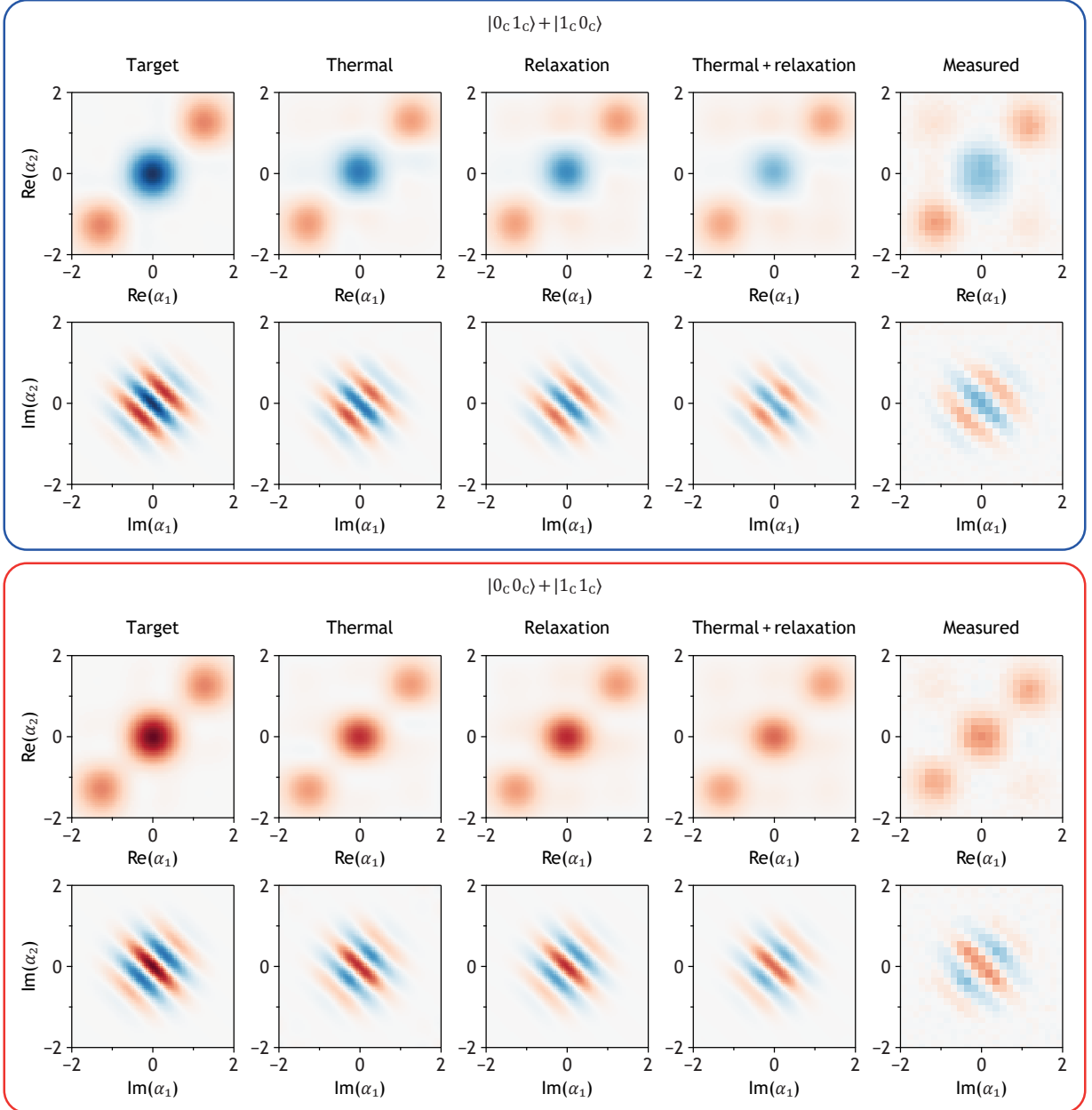
Equation (2) in the main text is obtained by setting $\Theta = -\pi/4$.

7. ELECTRONICS AND CABLING

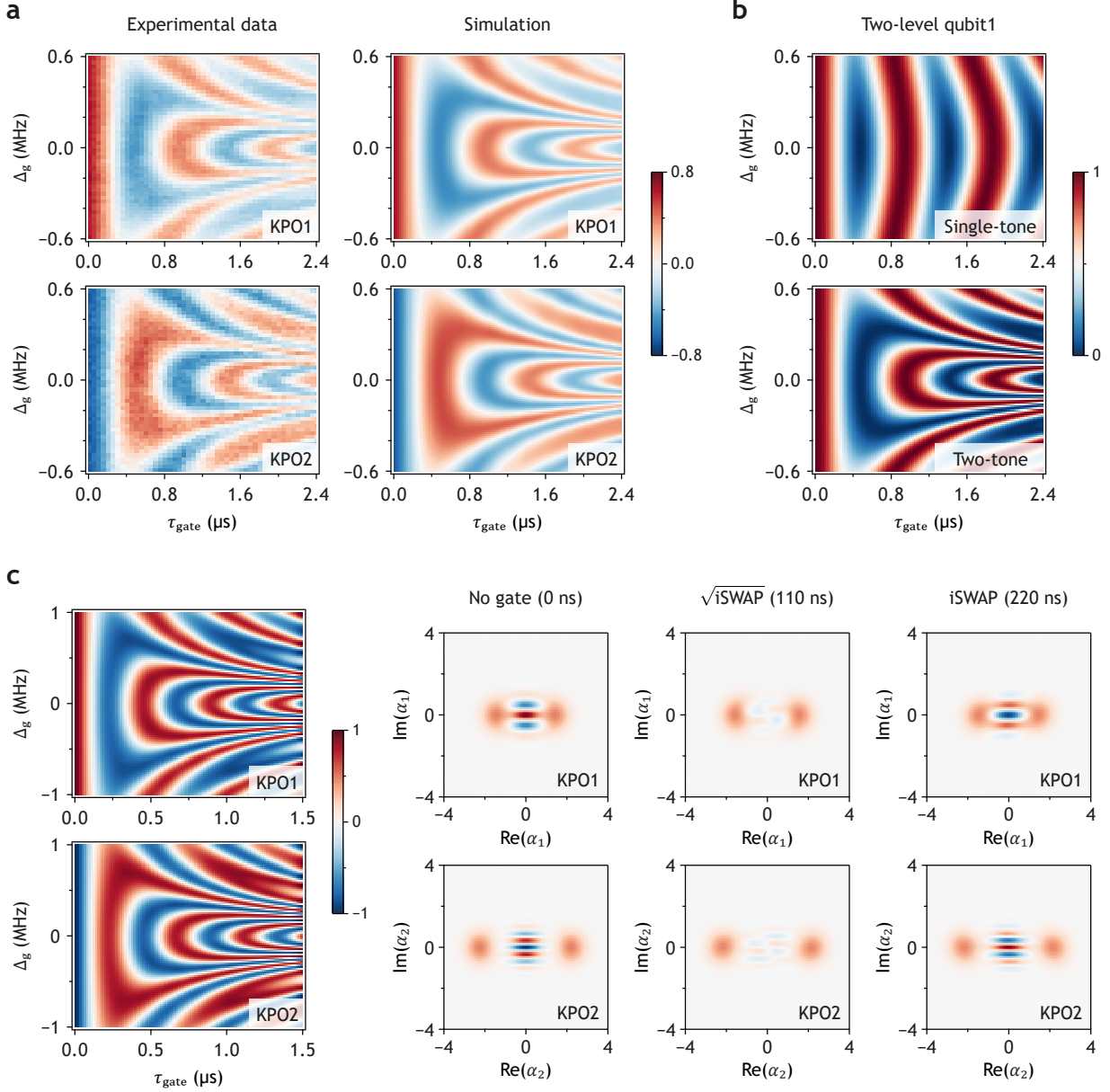
The pulses for the transmon and the readout resonator were generated by arbitrary waveform generators (AWGs), local oscillators, and IQ mixers. For the KPO, pulses were generated using Keysight M8195A (labelled ‘‘Fast AWG’’ in Supplementary Fig. 6a). This instrument has four channels, with each channel having two outputs, such as Ch. 1 and Ch. $\bar{1}$ (see the leftmost part of Supplementary Fig. 6a). The pulse shapes from these two outputs are identical, with only a 180° phase difference. In Ch. 1 (and Ch. $\bar{1}$), both the KPO1 drive and low-frequency pulses near the frequency $(\omega_{K1} - \omega_{K2})/2\pi = 144$ MHz are generated. The pulses from Ch. 1 pass through a bandpass filter to suppress the low-frequency component, while the pulses from Ch. $\bar{1}$ pass through multiple low-pass filters to cut out the gigahertz components. The KPO1 pump and the low-frequency pulses are combined in the mixing chamber and inserted into the KPO1 pump port of the chip (Fig. 1c).



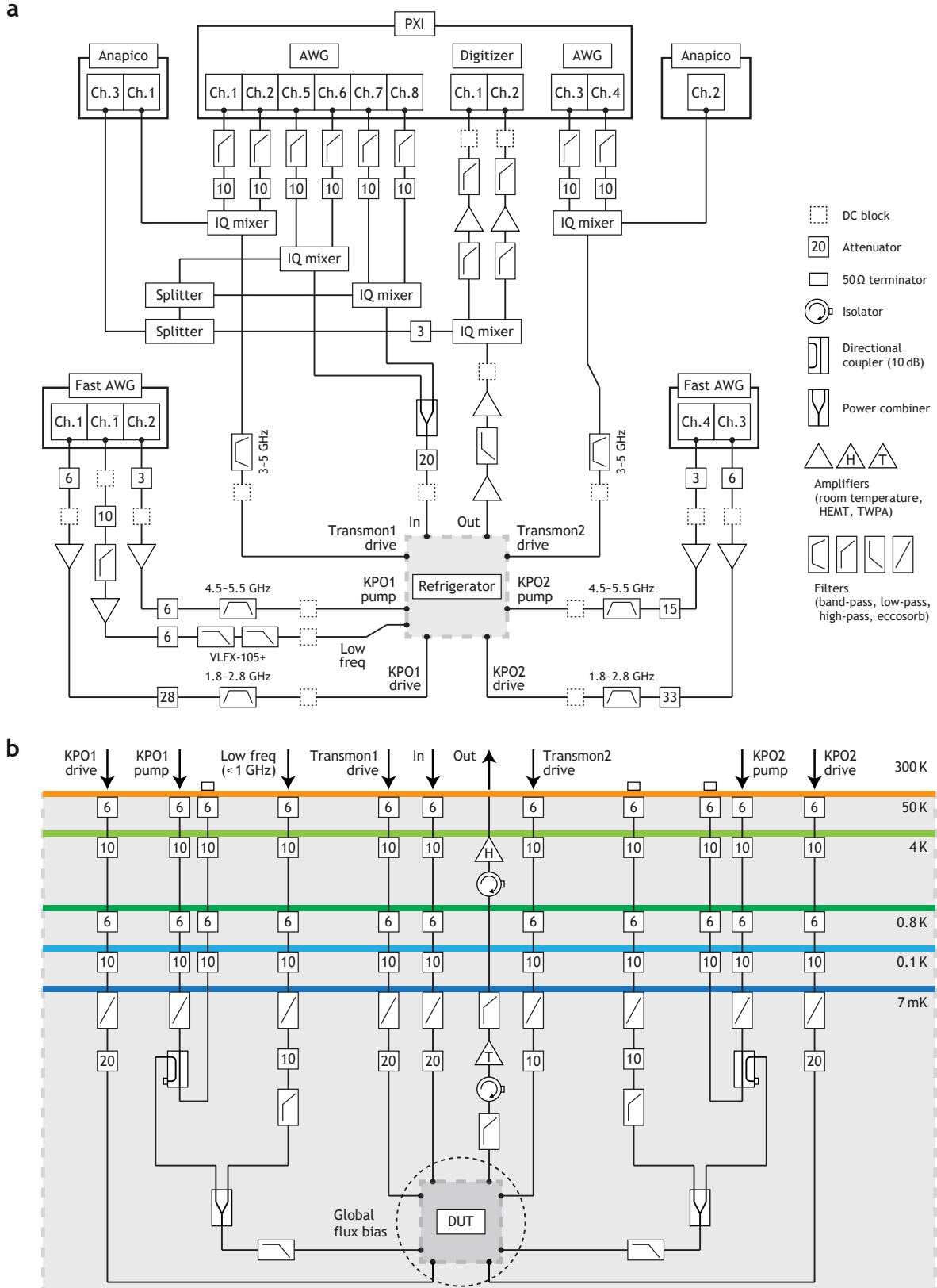
Supplementary Fig. 3: Two-mode Wigner functions of our target states. The cat states are eigenstates with the conditions $P_i = K_i$ and $\Delta_i = 0.5K_i$ ($i = 1, 2$). For Re-Re plots, $Im(\alpha_1) = Im(\alpha_2) = 0$, unless otherwise specified; for Im-Im plots, $Re(\alpha_1) = Re(\alpha_2) = 0$.



Supplementary Fig. 4: Two-mode Wigner functions for the target state (“Target”); simulated states with thermal states as initial states (“Thermal”), relaxation effects such as single-photon loss and dephasing (“Relaxation”), or both (“Thermal + relaxation”); and our measured results (“Measured”).



Supplementary Fig. 5: **a** Two-cat Rabi oscillations. The colours represent the number parity of each KPO. The gate amplitude from the fitting with the simulation is 2.96 MHz. In the simulation, both $T_1^{\text{K}1}$ and $T_1^{\text{K}2}$ were assumed 10 μs; dephasing was not considered. For more details, see Sec. 4B. **b** Simulation of Rabi oscillations in two interacting two-level qubits. The colours represent the population of the $|0\rangle$ state of qubit1. For this simulation, Supplementary Eqs. (9) (single tone) and (10) (two tones) with $J_m/2\pi = 1.06$ MHz were used. **c** Two-cat Rabi oscillations between two KPOs with different mean photon numbers. The mean photon number of KPO1 is 2.1, whereas that of KPO2 is 5.1. For the simulation, Supplementary Eqs. (3), (8), and (5) were used with the following conditions: The Kerr coefficient for both KPOs is 2 MHz; the pump amplitude and detuning for KPO1 are 3 MHz and 1 MHz, respectively; for KPO2, 8 MHz and 2 MHz, respectively. Relaxations are not considered in (b) and (c).



Supplementary Fig. 6: **a,b** Experimental configuration of room-temperature electronics (a) and cryogenic components (b). The 50- Ω -terminated port next to the pump line serves to dissipate unused pump power. The isolator at the mixing chamber is a double-junction isolator. The cables for the travelling-wave parametric amplifier (TWPA) pump are not shown for simplicity. A single instrument labelled “Fast AWG” is represented as two parts for ease of recognition; similarly, “Anapico”, which provides local oscillators, is shown in two parts.

SUPPLEMENTARY REFERENCES

- [1] X. You, J. A. Sauls, and J. Koch, *Circuit quantization in the presence of time-dependent external flux*, Phys. Rev. B **99**, 174512 (2019).
- [2] C. W. S. Chang, C. Sabín, P. Forn-Díaz, F. Quijandría, A. M. Vadiraj, I. Nsanzineza, G. Johansson, and C. M. Wilson, *Observation of Three-Photon Spontaneous Parametric Down-Conversion in a Superconducting Parametric Cavity*, Phys. Rev. X **10**, 011011 (2020).
- [3] W. Wyss, *Two Non-Commutative Binomial Theorems*, Preprint at <https://doi.org/10.48550/arXiv.1707.03861> (2017).
- [4] H. Chono, T. Kanao, and H. Goto, *Two-qubit gate using conditional driving for highly detuned Kerr nonlinear parametric oscillators*, Phys. Rev. Research **4**, 043054 (2022).
- [5] A. Essig, Q. Ficheux, T. Peronnin, N. Cottet, R. Lescanne, A. Sarlette, P. Rouchon, Z. Leghtas, and B. Huard, *Multiplexed Photon Number Measurement*, Phys. Rev. X **11**, 031045 (2021).
- [6] D. Iyama, T. Kamiya, S. Fujii, H. Mukai, Y. Zhou, T. Nagase, A. Tomonaga, R. Wang, J.-J. Xue, S. Watabe, S. Kwon, and J.-S. Tsai, *Observation and manipulation of quantum interference in a superconducting Kerr parametric oscillator*, Nat. Commun. **15**, 86 (2024).
- [7] L. G. Lutterbach and L. Davidovich, *Method for Direct Measurement of the Wigner Function in Cavity QED and Ion Traps*, Phys. Rev. Lett. **78**, 2547 (1997).
- [8] S. Haroche and J.-M. Raimond, *Exploring the Quantum: Atoms, Cavities, and Photons* (Oxford University Press, 2006).
- [9] B. Vlastakis, G. Kirchmair, Z. Leghtas, S. E. Nigg, L. Frunzio, S. M. Girvin, M. Mirrahimi, M. H. Devoret, and R. J. Schoelkopf, *Deterministically Encoding Quantum Information Using 100-Photon Schrödinger Cat States*, Science **342**, 607–610 (2013).
- [10] J. R. Johansson, P. D. Nation, and F. Nori, *QuTiP: An open-source Python framework for the dynamics of open quantum systems*, Comp. Phys. Comm. **183**, 1760–1772 (2012).
- [11] J. R. Johansson, P. D. Nation, and F. Nori, *QuTiP 2: A Python framework for the dynamics of open quantum systems*, Comp. Phys. Comm. **184**, 1234–1240 (2013).
- [12] S. Kwon, A. Tomonaga, G. L. Bhai, S. J. Devitt, and J.-S. Tsai, *Gate-based superconducting quantum computing*, J. Appl. Phys. **129**, 041102 (2021).